



OGLE-2018-BLG-1269Lb: A Jovian Planet with a Bright $I = 16$ Host

Youn Kil Jung^{1,29}, Andrew Gould^{1,2,3,29}, Andrzej Udalski^{4,30}, Takahiro Sumi^{5,31}, Jennifer C. Yee^{6,29}, Cheongho Han^{7,29},
and

Michael D. Albrow⁸, Sun-Ju Chung^{1,9}, Kyu-Ha Hwang¹, Yoon-Hyun Ryu¹, In-Gu Shin¹, Yossi Shvartzvald¹⁰,
Wei Zhu¹¹, Weicheng Zang¹², Sang-Mok Cha^{1,13}, Dong-Jin Kim¹, Hyoun-Woo Kim¹, Seung-Lee Kim^{1,9},
Chung-Uk Lee^{1,9}, Dong-Joo Lee¹, Yongseok Lee^{1,13}, Byeong-Gon Park^{1,9}, Richard W. Pogge²

(The KMTNet Collaboration),

Przemek Mróz^{4,14}, Michał K. Szymański⁴, Jan Skowron⁴, Radek Poleski^{2,4}, Igor Soszyński⁴, Paweł Pietrukowicz⁴,
Szymon Kozłowski⁴, Krzysztof Ulaczyk¹⁵, Krzysztof A. Rybicki⁴, Patryk Iwanek⁴, Marcin Wrona⁴

(The OGLE Collaboration),

and

Fumio Abe¹⁶, Richard Barry¹⁷, David P. Bennett^{17,18}, Ian A. Bond¹⁹, Aparna Bhattacharya^{17,18}, Martin Donachie²⁰,
Akihiko Fukui^{21,22}, Yuki Hirao⁵, Yoshitaka Itow¹⁶, Iona Kondo⁵, Naoki Koshimoto^{23,24}, Man Cheung Alex Li²⁰,
Yutaka Matsubara¹⁶, Shota Miyazaki⁵, Yasushi Muraki¹⁶, Masayuki Nagakane⁵, Clément Ranc¹⁷, Nicholas J. Rattenbury²⁰,
Haruno Suematsu⁵, Denis J. Sullivan²⁵, Daisuke Suzuki²⁶, Paul J. Tristram²⁷, and Atsunori Yonehara²⁸

(The MOA Collaboration)

¹ Korea Astronomy and Space Science Institute, Daejeon 34055, Republic of Korea

² Department of Astronomy, Ohio State University, 140 W. 18th Ave., Columbus, OH 43210, USA

³ Max-Planck-Institute for Astronomy, Königstuhl 17, D-69117 Heidelberg, Germany

⁴ Warsaw University Observatory, Al. Ujazdowskie 4, 00-478 Warszawa, Poland

⁵ Department of Earth and Space Science, Graduate School of Science, Osaka University, Toyonaka, Osaka 560-0043, Japan

⁶ Center for Astrophysics|Harvard & Smithsonian, 60 Garden St., Cambridge, MA 02138, USA

⁷ Department of Physics, Chungbuk National University, Cheongju 28644, Republic of Korea

⁸ University of Canterbury, Department of Physics and Astronomy, Private Bag 4800, Christchurch 8020, New Zealand

⁹ University of Science and Technology, Korea, 217 Gajeong-ro Yuseong-gu, Daejeon 34113, Republic of Korea

¹⁰ IPAC, Mail Code 100-22, Caltech, 1200 E. California Blvd., Pasadena, CA 91125, USA

¹¹ Canadian Institute for Theoretical Astrophysics, University of Toronto, 60 St George St., Toronto, ON M5S 3H8, Canada

¹² Physics Department and Tsinghua Centre for Astrophysics, Tsinghua University, Beijing 100084, People's Republic of China

¹³ School of Space Research, Kyung Hee University, Yongin 17104, Republic of Korea

¹⁴ Division of Physics, Mathematics, and Astronomy, California Institute of Technology, Pasadena, CA 91125, USA

¹⁵ Department of Physics, University of Warwick, Gibbet Hill Rd., Coventry, CV4 7AL, UK

¹⁶ Institute for Space-Earth Environmental Research, Nagoya University, Nagoya 464-8601, Japan

¹⁷ Code 667, NASA Goddard Space Flight Center, Greenbelt, MD 20771, USA

¹⁸ Department of Astronomy, University of Maryland, College Park, MD 20742, USA

¹⁹ Institute of Natural and Mathematical Science, Massey University, Auckland 0745, New Zealand

²⁰ Department of Physics, University of Auckland, Private Bag 92019, Auckland, New Zealand

²¹ Department of Earth and Planetary Science, Graduate School of Science, The University of Tokyo, 7-3-1 Hongo, Bunkyo-ku, Tokyo 113-0033, Japan

²² Instituto de Astrofísica de Canarias, Vía Láctea s/n, E-38205 La Laguna, Tenerife, Spain

²³ Department of Astronomy, Graduate School of Science, The University of Tokyo, 7-3-1 Hongo, Bunkyo-ku, Tokyo 113-0033, Japan

²⁴ National Astronomical Observatory of Japan, 2-21-1 Osawa, Mitaka, Tokyo 181-8588, Japan

²⁵ School of Chemical and Physical Science, Victoria University, Wellington, New Zealand

²⁶ Institute of Space and Astronautical Science, Japan Aerospace Exploration Agency, Kanagawa 252-5210, Japan

²⁷ University of Canterbury Mt. John Observatory, P.O. Box 56, Lake Tekapo 8770, New Zealand

²⁸ Department of Physics, Faculty of Science, Kyoto Sangyo University, Kyoto 603-8555, Japan

Received 2020 June 28; revised 2020 July 26; accepted 2020 August 1; published 2020 September 2

Abstract

We report the discovery of a planet in the microlensing event OGLE-2018-BLG-1269 with a planet–host mass ratio $q \sim 6 \times 10^{-4}$, i.e., 0.6 times smaller than the Jupiter/Sun mass ratio. Combined with the Gaia parallax and proper motion, a strong one-dimensional constraint on the microlens parallax vector allows us to significantly reduce the uncertainties of lens physical parameters. A Bayesian analysis that ignores any information about light from the host yields that the planet is a cold giant ($M_2 = 0.69^{+0.44}_{-0.22} M_J$) orbiting a Sun-like star ($M_1 = 1.13^{+0.72}_{-0.35} M_\odot$) at a distance of $D_L = 2.56^{+0.92}_{-0.62}$ kpc. The projected planet–host separation is $a_L = 4.61^{+1.70}_{-1.17}$ au. Using Gaia astrometry, we show that the blended light lies $\lesssim 12$ mas from the host and therefore must be either the host star or a stellar companion to the host. An isochrone analysis favors the former possibility at $>99.6\%$. The host is therefore a subgiant. For host metallicities in the range of $0.0 \leq [\text{Fe}/\text{H}] \leq +0.3$, the host and planet masses are then in the range of $1.16 \leq M_1/M_\odot \leq 1.38$ and $0.74 \leq M_2/M_J \leq 0.89$, respectively. Low host metallicities are excluded. The brightness

²⁹ The KMTNet Collaboration.

³⁰ The OGLE Collaboration.

³¹ The MOA Collaboration.

and proximity of the lens make the event a strong candidate for spectroscopic follow-up both to test the microlensing solution and to further characterize the system.

Unified Astronomy Thesaurus concepts: [Gravitational microlensing \(672\)](#); [Gravitational microlensing exoplanet detection \(2147\)](#)

Supporting material: data behind figure

1. Introduction

Although microlensing events have been repeatedly observed toward the Galactic bulge field, only a few tests of the microlensing solutions have been possible. This is mainly because microlensing is an inherently rare phenomenon, and the lensing objects are often very faint. A microlensing event occurs when two stars at different distances (a foreground lens and a background source) are aligned to within of order 1 mas along the line of sight. This suggests that even in the densest field of the sky (i.e., the Galactic center), only about one among a million stars is likely to undergo a microlensing event at a given moment (Griest et al. 1991; Paczyński 1991). In addition, these events are, in most cases, not repeating and relatively brief ($t_E \sim 20$ days, where t_E is the Einstein timescale). While microlensing is sensitive to any lenses distributed along the galactocentric distance, the most typical lens stars are M dwarfs because they are the most common population of stars in the Galaxy. Hence, the lenses are usually very faint (with absolute magnitudes of $M_I \sim 8$). Considering that microlensing observations are conducted toward crowded fields in which stellar images are severely blended, the faintness of the lens makes it challenging to make follow-up observations of the lens after the event is over. As a result, there exist only a few cases in which the solutions for the lenses are checked by follow-up observations.

The most explicit way to check the microlensing solution is to directly observe the lens with high-resolution imaging. For typical lensing events, the lens proper motion relative to the source is $\mu \sim 5$ mas yr⁻¹. This suggests that for direct lens imaging with currently available high-resolution instruments, one needs to wait ~ 10 – 20 yr until the lens is separated sufficiently from the source. As a result, this test has been done only for a limited number of events (Alcock et al. 2001; Kozłowski et al. 2007; Batista et al. 2015; Bennett et al. 2015, 2020; Bhattacharya et al. 2018; Vanderou et al. 2020).

An alternative way to test the microlensing solution regardless of the lens–source motion is to conduct spectroscopic observations (Han et al. 2019). Such an observation may enable one to directly measure the lens spectral type from spectroscopic information, such as temperature, surface gravity, and metallicity. Then, one can check the solution by comparing the measured spectral type with the prediction from photometric data. However, this method can only be applied provided that the lens is bright enough to be spectroscopically resolved at high contrast with the source and unrelated neighbors.

The microlensing solution can be checked by radial velocity (RV) observations (Yee et al. 2016). However, measuring the RV signal for a typical lens is very difficult because of its faintness and its slow motion relative to the source. In such conditions, the light from the lens is usually contaminated by blended light, which will significantly dilute the signal from the target of interest. For the same reason, the RV observations for stellar lenses with planetary companions will be further complicated because their expected RVs (\mathcal{O} m s⁻¹) are much smaller than those of stellar binaries (\mathcal{O} km s⁻¹). Therefore, the

RV measurement on a microlensing target also requires a rare lens that is close to us and/or bright enough to be clearly visible in the blended light.

In rare cases for which the lens is bright, the microlensing solution can also be checked by analyzing the light curve acquired from photometric observations. For solutions with a measured lens mass M and a distance D_L , one can estimate the color and brightness of the lens. If these estimates are close to the blended light, it is likely that the lens flux comprises a significant portion of the blended flux (Han et al. 2018). Because the lens is bright, it can then be observed in high-resolution images as an additional light blended with the source flux. Hence, one can check the solution by identifying the lens from the excess flux. For example, Bennett et al. (2010) observed the multiple planetary event OGLE-2006-BLG-109 (Gaudi et al. 2008) using Keck adaptive optics (AO) and confirmed that the light from the lens measured from high-resolution images is consistent with that predicted from modeling.

Here we present an analysis of OGLE-2018-BLG-1269. The event was generated by a cold giant planet orbiting a Sun-like star, i.e., with a planet–host mass ratio of $q = M_2/M_1 \sim 6 \times 10^{-4}$. The planetary perturbation was densely covered by the Korea Microlensing Telescope Network (KMTNet; Kim et al. 2016), and the parallax and proper motion of the baseline object were independently measured by Gaia (Gaia Collaboration et al. 2016, 2018). A Bayesian analysis suggests that the planet is close to us and the host is associated with the blended light. These make the event a strong candidate for high-resolution imaging, as well as 10 and 30 m spectroscopic observations to test the microlensing solution and further characterize this planetary system.

2. Observation

The event OGLE-2018-BLG-1269, (R.A., decl.)_{J2000} = (17:58:46.42, $-27:37:04.6$), or $(l, b) = (2^\circ 61', -1^\circ 82')$ in Galactic coordinates, was first discovered on July 12 by the Optical Gravitational Lensing Experiment (OGLE; Udalski et al. 2015) survey and alerted by its Early Warning System (Udalski 2003). The event was in the OGLE BLG504.27 field with a nominal cadence of 10 times night⁻¹ using the 1.3 m Warsaw Telescope located at the Las Campanas Observatory in Chile. The apparent I -band magnitude of the baseline object is $I_{\text{base}} \sim 15.8$. We note that, as will be discussed in Section 4, the microlensed source is heavily blended, and only $\sim 4\%$ of the baseline flux comes from the source.

This event was independently found on August 5 by the Microlensing Observations in Astrophysics (MOA; Sumi et al. 2003) survey. In the MOA alert system (Bond et al. 2001), it was listed as MOA-2018-BLG-293. The MOA survey monitored the event with a 15 minute cadence using the 1.8 m MOA-II telescope located at Mt. John Observatory in New Zealand.

The KMTNet survey also discovered the event from its annual postseason analysis (Kim et al. 2018) and cataloged it as KMT-2018-BLG-2418. This survey used three 1.6 m telescopes that are distributed over three different continents, i.e.,

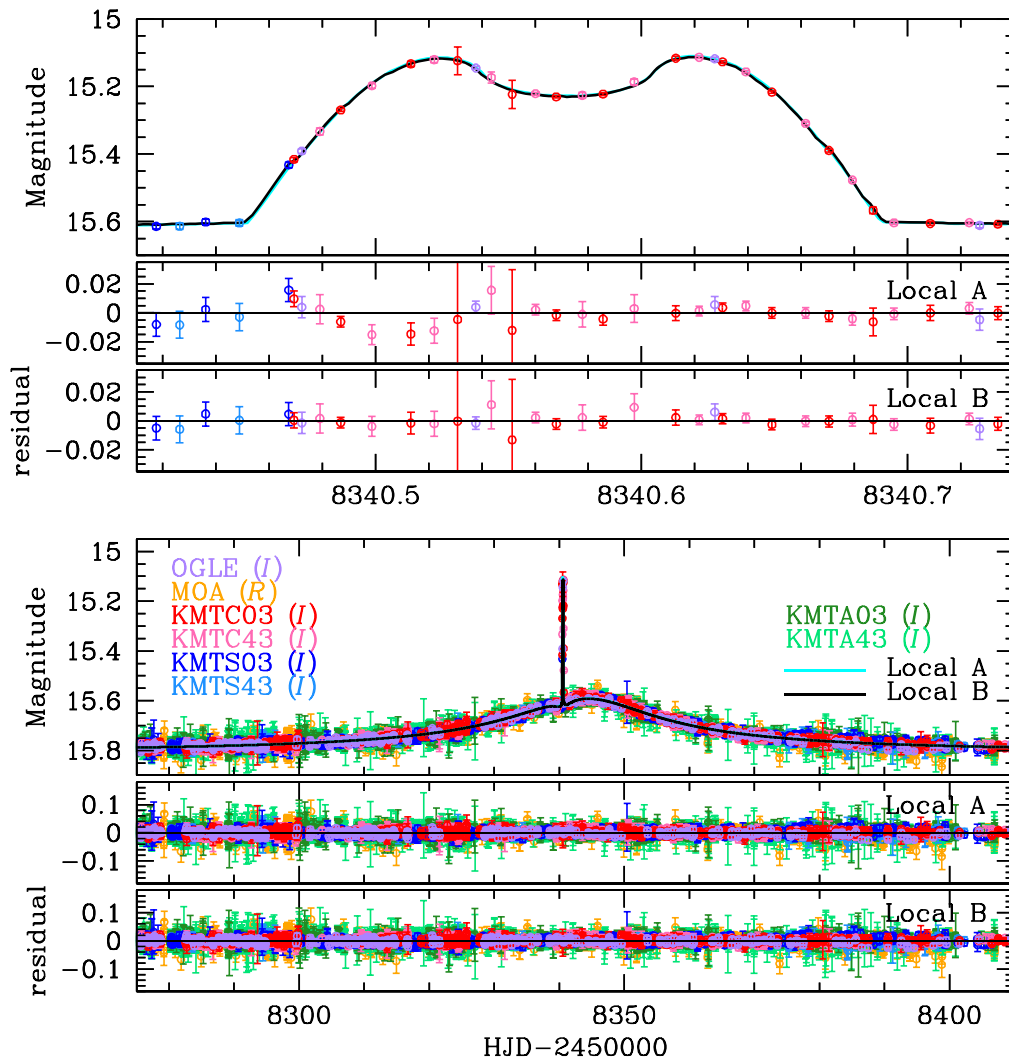


Figure 1. Light curve of OGLE-2018-BLG-1269. The upper panel shows a zoom of the short-term anomaly centered at $\text{HJD}' \sim 8340.58$. The cyan and black curves are the best-fit models from Table 1.

(The data used to create this figure are available.)

Chile (KMTA), South Africa (KMTS), and Australia (KMTA). The event was in two offset fields (BLG03 and BLG43) and thus was monitored with the cadence of four times hr^{-1} .

The OGLE and KMTNet images were primarily obtained in the I band, while some V -band images were taken solely to measure the source color. The MOA images were obtained in a customized R band, which is approximately the sum of the standard R and I bands. These data were then reduced using the pipelines of the survey groups (Woźniak 2000; Bond et al. 2001; Albrow et al. 2009), which are variants of difference image analysis (DIA; Tomaney & Crotts 1996; Alard & Lupton 1998).

3. Light-curve Analysis

Figure 1 shows the light curve of OGLE-2018-BLG-1269. This light curve mostly follows a standard Paczyński (1986) curve, except for the very short time interval $8,340.4 < \text{HJD}' (= \text{HJD} - 2,450,000) < 8,340.8$, during which OGLE and KMTA observations caught a strong anomaly consisting of two strong spikes with a U-shaped trough. Such an anomaly typically occurs when a source crosses a pair of caustics formed

by a binary lens with $q \ll 1$, i.e., a planetary system. Hence, we fit the light curve with the binary-lens single-source (2L1S) model.

In cases of standard 2L1S models, the lensing magnification, $A(t)$, can be described by seven nonlinear parameters. The first three are the geometric parameters (t_0 , u_0 , t_E): the time of closest lens–source approach, the impact parameter (scaled to the angular Einstein radius θ_E), and the timescale, respectively. The next three (s , q , α) are the parameters that describe the binarity of the lens: the projected companion–host separation (scaled to θ_E), their mass ratio, and their orientation angle (relative to the source trajectory), respectively. The last parameter is the source radius $\rho = \theta_*/\theta_E$, where θ_* is the angular source radius.

With these nonlinear parameters, we perform a systematic 2L1S analysis by adopting the modeling procedure of Jung et al. (2015). We first derive initial estimates of (t_0 , u_0 , t_E) by fitting the single-lens single-source (1L1S) model to the event with the anomaly excluded. We also derive an initial estimate of $\rho = 8 \times 10^{-4}$ based on the source brightness and t_E from the 1L1S fit. Next, we carry out a dense search over a grid of s ,

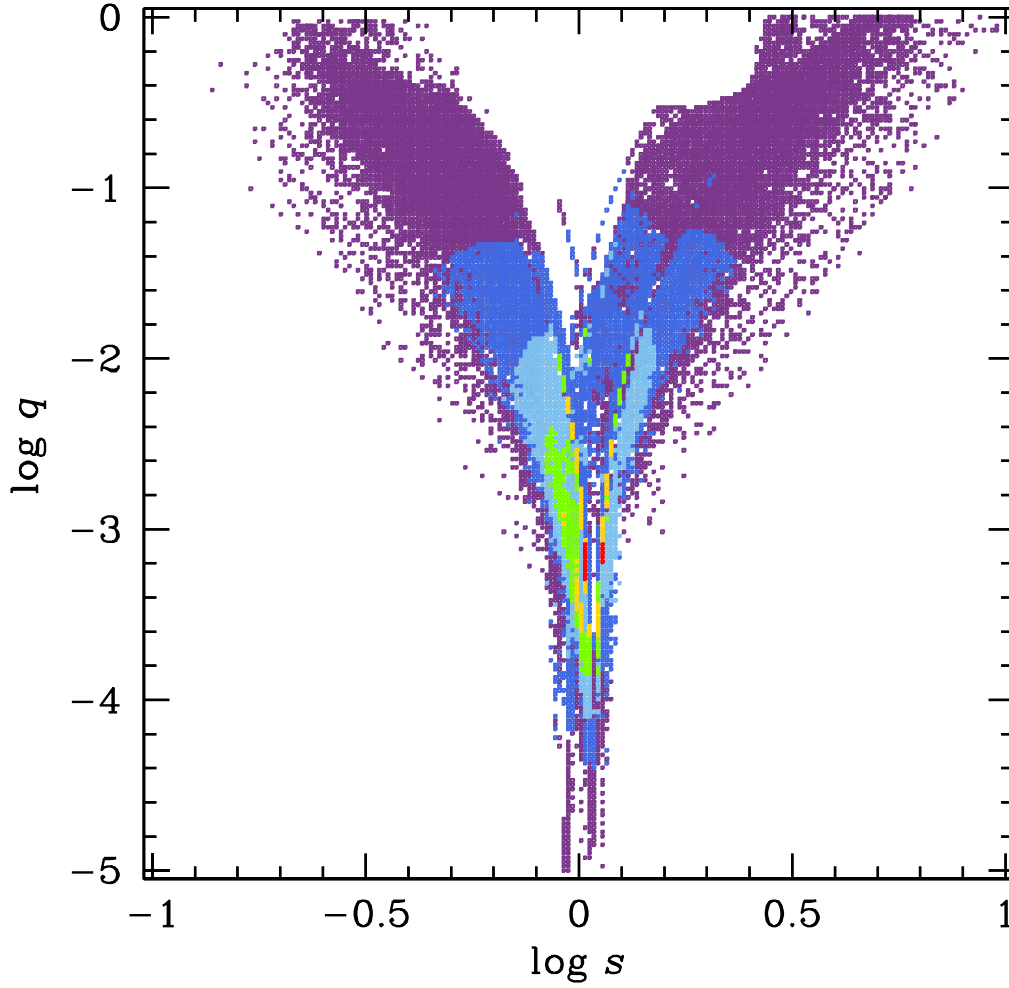


Figure 2. The $\Delta\chi^2$ map in the $(\log s, \log q)$ plane derived from the grid search. The six colors (red, yellow, green, light blue, dark blue, and purple) represent the grid with $\Delta\chi^2 < [(1n)^2, (2n)^2, (3n)^2, (4n)^2, (5n)^2, (6n)^2]$, where $n = 40$.

Table 1
Lensing Parameters

Parameters	Local A		Local B	
	Standard	Standard	Orbit+Parallax	
			$u_0 > 0$	$u_0 < 0$
$\chi^2_{\text{tot}}/\text{dof}$	22,256.3/21,841	22,229.4/21,841	22,221.2/21,837	22,222.1/21,837
t_0 (HJD')	$8,343.876 \pm 0.025$	$8,343.849 \pm 0.025$	$8,343.903 \pm 0.030$	$8,343.895 \pm 0.029$
u_0	0.141 ± 0.026	0.142 ± 0.023	0.144 ± 0.028	-0.143 ± 0.024
t_E (days)	70.792 ± 1.064	70.584 ± 0.923	70.672 ± 1.661	69.597 ± 1.172
s	1.032 ± 0.019	1.126 ± 0.012	1.123 ± 0.032	1.124 ± 0.033
q (10^{-4})	5.940 ± 0.063	5.932 ± 0.066	5.753 ± 0.264	5.957 ± 0.230
α (rad)	1.888 ± 0.026	1.887 ± 0.026	1.887 ± 0.069	-1.891 ± 0.068
ρ (10^{-4})	5.886 ± 0.097	5.917 ± 0.092	5.895 ± 0.177	5.941 ± 0.130
$\pi_{E,N}$	0.171 ± 0.150	0.114 ± 0.173
$\pi_{E,E}$ (10^{-1})	0.086 ± 0.217	0.253 ± 0.107
ds/dt (yr^{-1})	-0.287 ± 0.319	-0.219 ± 0.298
$d\alpha/dt$ (yr^{-1})	0.032 ± 0.554	0.205 ± 0.492
f_s	0.270 ± 0.006	0.270 ± 0.005	0.275 ± 0.007	0.273 ± 0.006
f_b	7.303 ± 0.006	7.304 ± 0.005	7.299 ± 0.007	7.301 ± 0.006

q , and α . For this, we divide the parameter space into $200 \times 200 \times 21$ grids in the range of $-1 < \log s < 1$, $-5 < \log q < 0$, and $0 < \alpha < 2\pi$, respectively. At each $(\log s, \log q, \alpha)$ grid point, we fix $(\log s, \log q)$ and then fit

the light curve by allowing the remaining parameters ($t_0, u_0, t_E, \alpha, \rho$) to vary in a Markov Chain Monte Carlo (MCMC).

We identify two local minima in the resulting $\Delta\chi^2$ map in the $(\log s, \log q)$ plane (see Figure 2). We then further

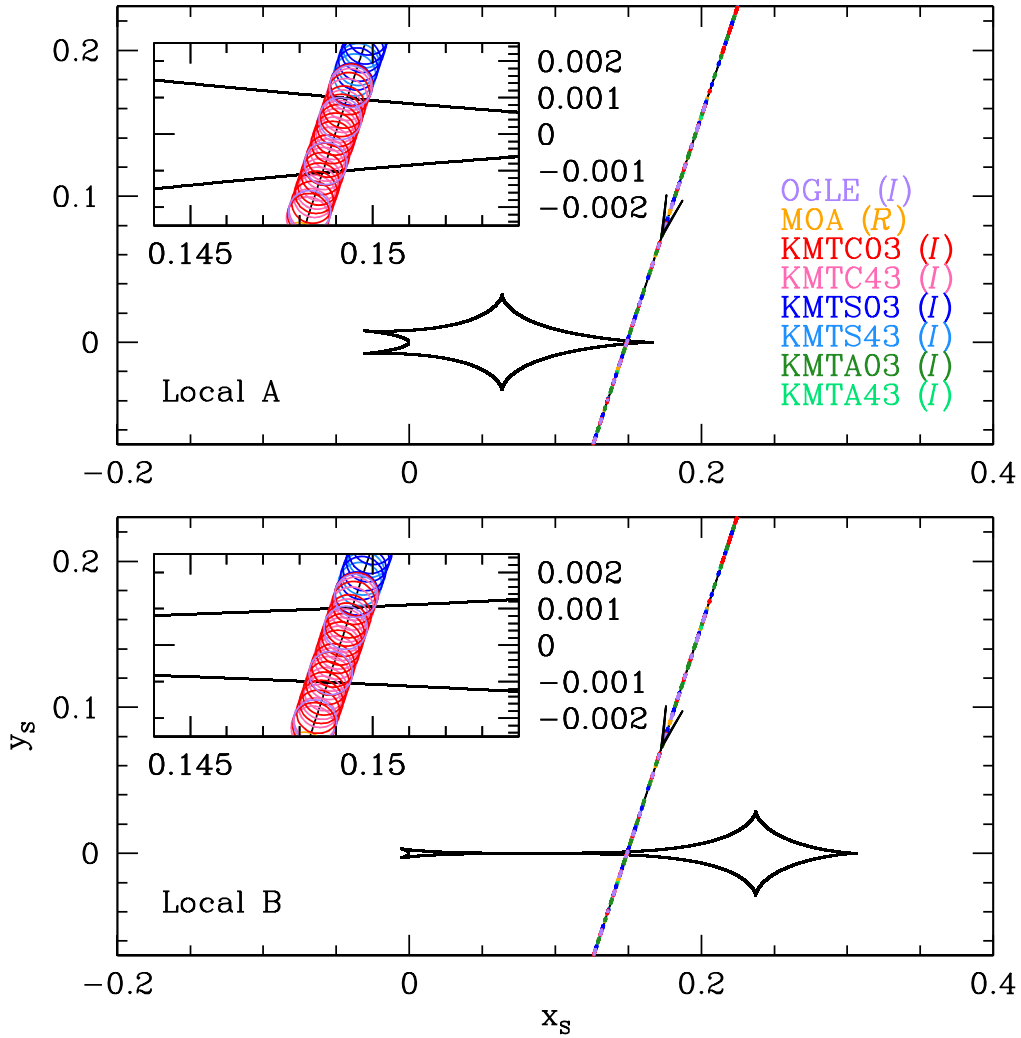


Figure 3. Caustic structures for the two solutions. In each panel, the black curve is the source trajectory, and the open circles on the trajectory (scaled by the source radius ρ) are the source locations at the times of observation. The inset shows the zoom of the caustic crossing region.

refine these minima by optimizing all fitting parameters and finally find that they converge to the two points, i.e., $(s, q) = (1.03, 5.94 \times 10^{-4})$ and $(1.13, 5.93 \times 10^{-4})$. See Table 1. The MCMC results show that the best-fit parameters of the two solutions are consistent within 1σ (except for the separation s). However, the solution Local A ($s = 1.03$) is disfavored relative to the solution Local B ($s = 1.13$) by $\Delta\chi^2 = 27$. In addition, the former solution has clear systematic residuals in the short-lived anomaly region, as presented in the upper panel of Figure 1. Therefore, we exclude the Local A solution. The caustic structures for the two solutions are shown in Figure 3.

The timescale of the standard solution ($t_E \sim 71$ days) comprises a substantial portion of Earth’s orbital period. Hence, we additionally check whether the standard fit further improves by introducing the microlens parallax (Gould 1992, 2000),

$$\pi_E \equiv \pi_E \frac{\mu_{\text{rel}}}{\mu_{\text{rel}}}; \pi_E = \frac{\pi_{\text{rel}}}{\theta_E}, \quad (1)$$

where $(\mu_{\text{rel}}, \pi_{\text{rel}})$ are the relative lens source (geocentric proper motion, parallax). To account for the parallax, we add two

parameters $(\pi_{E,N}, \pi_{E,E})$ to the standard model, i.e., the north and east components of π_E in equatorial coordinates. Note that the measurements of θ_E and π_E allow one to determine the lens total mass M and distance D_L through the relations

$$M = \frac{\theta_E}{\kappa\pi_E}; D_L = \frac{\text{au}}{\pi_E\theta_E + \pi_S}, \quad (2)$$

where $\kappa = 4G/(c^2\text{au}) \sim 8.14 \text{ mas } M_\odot^{-1}$, $\pi_S = \text{au}/D_S$ is the source parallax, and D_S is the source distance. Then, one can further determine the lens physical properties (M_1, M_2, a_\perp) from the measured s and q , where $a_\perp = sD_L\theta_E$ is the physical projected companion–host separation.

In order to check the feasibility of measuring the microlensing parallax, we conduct an additional modeling considering the effect. This modeling yields a solution that provides a minor fit improvement, by $\Delta\chi^2 \sim 7$, relative to the standard model. The measured parallax parameters are not much more than the measurement uncertainties. Considering the subtlety of the effect, determining $\pi_{E,N}$ and $\pi_{E,E}$ might be affected by the lens orbital motion that is known to affect π_E measurements (Batista et al. 2011). Therefore, we conduct an additional modeling in which both the microlens parallax and lens orbital

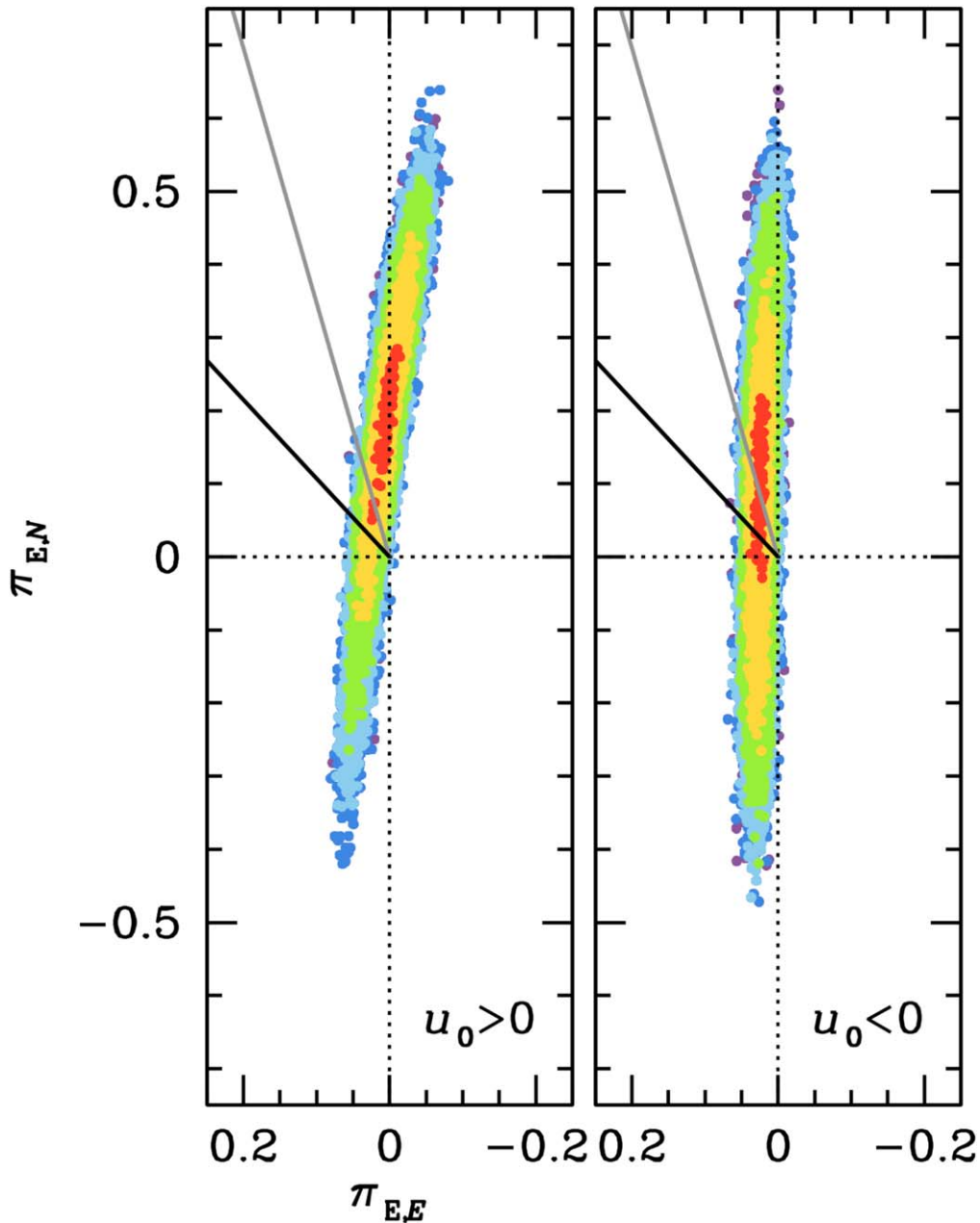


Figure 4. The $\Delta\chi^2$ maps in the $(\pi_{E,N}, \pi_{E,E})$ plane obtained from the two solutions ($u_0 > 0$ and $u_0 < 0$). Except for $n = 1$, the color notation is identical to that of Figure 2. The two rays in each panel at $\phi = 16^\circ$ (gray) and 43° (black) represent the 1σ range of the direction of the lens–source relative motion that is derived within the Bayesian analysis. See the final paragraph of Section 4. It is the imposition of this constraint on the 1D parallax contours in this figure that forces the two solutions to have very similar and relatively small mass ranges.

effects are simultaneously considered. To account for the orbital effect, we add two extra parameters of $(ds/dt, d\alpha/dt)$, which are the instantaneous change rates of s and α , respectively (Dominik 1998). This modeling yields a negligible fit improvement from the parallax model, and the measured parallax parameters are almost unchanged from those of the parallax-only solution, indicating that the parallax effect is the dominant higher-order effect over the lens orbital effect.

The results are listed in Table 1. We find that the addition of higher-order effects does not significantly improve the fit, which only provides $\Delta\chi^2 \sim 8$. This implies that it is difficult to characterize the lens system from the fitted parallax parameters alone. Hence, we make a Bayesian analysis with

Galactic model priors to constrain the lens physical parameters. Nevertheless, despite the low level of fit improvement, the analysis gives a strong one-dimensional (1D) constraint on the parallax vector π_E , as seen in Figure 4. The short direction of these contours corresponds to the direction of Earth’s instantaneous acceleration at t_0 , namely $\psi = 266.7^\circ$ (north through east), which induces an approximately antisymmetric distortion on the light curve around t_0 . In addition, the seven standard parameters are comparable between all the solutions (including the standard solution), with the exception of the sign of u_0 . Therefore, we take the measured microlens parallax into consideration in our Bayesian analysis (e.g., Jung et al. 2019).

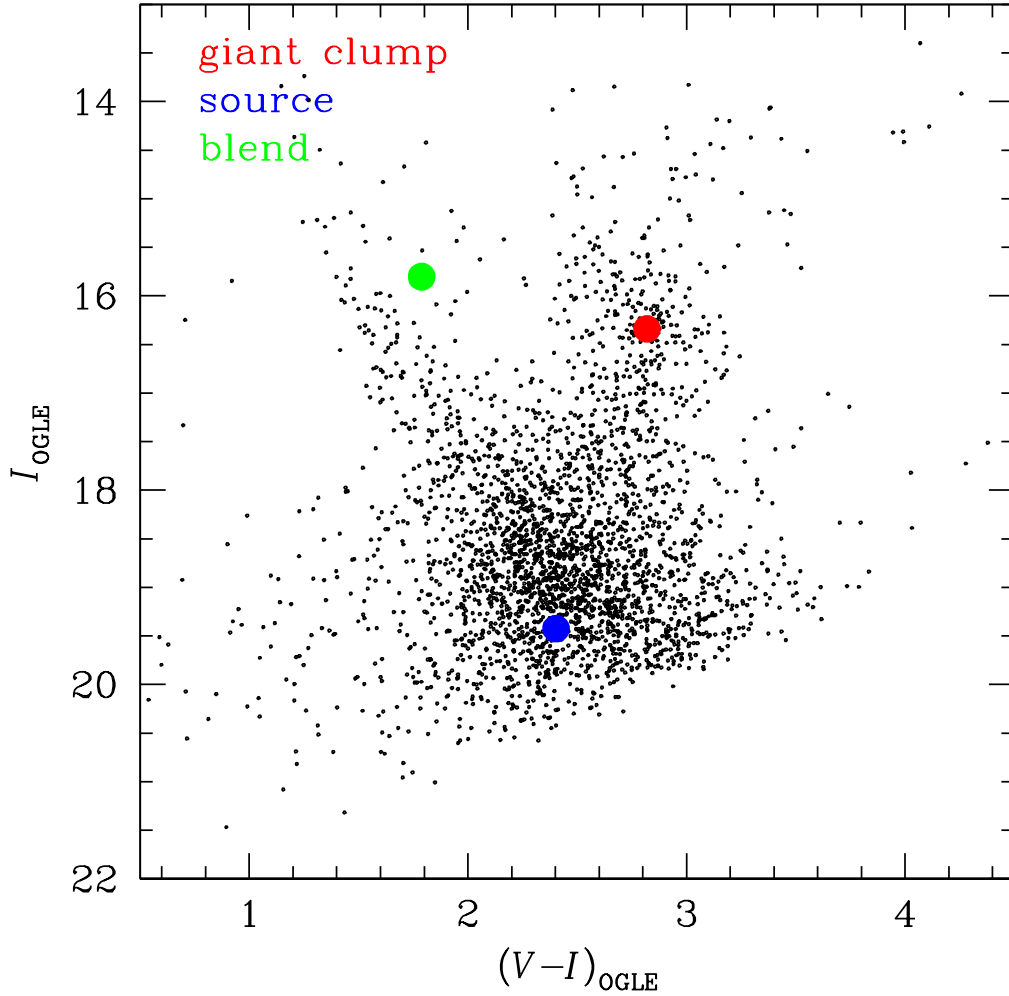


Figure 5. The CMD for stars around OGLE-2018-BLG-1269 obtained from the KMTC03 pyDIA reduction calibrated to OGLE-III photometry. The locations of the microlensed source, the centroid of the GC, and the blended light are marked by blue, red, and green circles, respectively.

4. Physical Parameter Estimates

4.1. Color-Magnitude Diagram

The normalized source radius ρ is precisely measured (see Table 1). This implies that we can measure $\theta_E = \theta_*/\rho$ provided that we can estimate the angular source radius θ_* . The Einstein radius is related to the lens mass M and the relative parallax π_{rel} by

$$\theta_E \equiv \sqrt{\kappa M \pi_{\text{rel}}}; \quad \pi_{\text{rel}} = \text{au} \left(\frac{1}{D_L} - \frac{1}{D_S} \right). \quad (3)$$

Then, we can use the measured θ_E to constrain the lens properties. Hence, we first estimate θ_* by following the approach of Yoo et al. (2004).

Based on the KMTC03 pyDIA reduction calibrated to the OGLE-III catalog (Szymański et al. 2011), we build a $(V-I, I)$ color-magnitude diagram (CMD) with stars centered on the event location (see Figure 5). We next find the source position of $(V-I, I)_S = (2.40 \pm 0.02, 19.42 \pm 0.01)$ from the best-fit model. We also estimate the giant clump (GC) centroid as $(V-I, I)_{\text{GC}} = (2.82 \pm 0.05, 16.34 \pm 0.07)$, which yields an

offset

$$\begin{aligned} \Delta(V-I, I) &= (V-I, I)_{\text{GC}} - (V-I, I)_{0,\text{GC}} \\ &= (1.76 \pm 0.05, 1.98 \pm 0.07), \end{aligned} \quad (4)$$

where $(V-I, I)_{0,\text{GC}} = (1.06, 14.36)$ is the intrinsic GC centroid (Bensby et al. 2013; Nataf et al. 2013). Using this offset, we obtain the dereddened source position as $(V-I, I)_{0,S} = (V-I, I)_S - \Delta(V-I, I) = (0.64 \pm 0.05, 17.44 \pm 0.07)$. This suggests that the source is either a late F or an early G dwarf.

We then apply $(V-I, I)_{0,S}$ to the VIK (Bessell & Brett 1988) and $(V-K)/\theta_*$ (Kervella et al. 2004) relations to derive

$$\theta_* = 0.948 \pm 0.068 \mu\text{as}, \quad (5)$$

where we add 5% error in quadrature to θ_* to account for the uncertainty of $(V-I, I)_{0,\text{GC}}$ and the color/surface brightness conversion of the Galactic bulge population relative to locally calibrated stars. With the measured ρ , we obtain

$$\theta_E = 1.602 \pm 0.118 \text{ mas}. \quad (6)$$

The geocentric relative lens–source proper motion is then

$$\mu_{\text{rel}} = \frac{\theta_E}{t_E} = 8.29 \pm 0.61 \text{ mas yr}^{-1}. \quad (7)$$

The unusually large values of θ_E and μ_{rel} suggest that the lens lies in the Galactic disk. From the definition of θ_E (Equation (3)),

$$\pi_{\text{rel}} = 0.22 \text{ mas} \left(\frac{\theta_E}{1.6 \text{ mas}} \right)^2 \left(\frac{M}{1.4 M_\odot} \right)^{-1}. \quad (8)$$

Thus, given the lens flux constraint, which will be discussed in the following subsection, the lens must be $D_L = au/(\pi_{\text{rel}} + \pi_S) \lesssim 3 \text{ kpc}$ (unless the lens is a black hole). We note that the measured μ_{rel} is also consistent with the typical values of disk lenses.

4.2. Gaia PPPM of Baseline Object

Gaia data (Gaia Collaboration et al. 2016, 2018; Luri et al. 2018) will play a critical role in the derivation of the lens physical characteristics in several different respects. As has become relatively common in recent years, we will make use of the Gaia proper-motion measurement of the “baseline object.” However, in contrast to most events with such a measurement, in this case, the baseline object is strongly dominated by the lens (or at least a stellar component of the lens system). Thus, the Gaia parallax measurement is also relevant.³² Moreover, in this paper, for the first time, we will make use of the Gaia position measurement of the baseline object. That is, we will use the full position, parallax, proper-motion (PPPM) Gaia solution at various points in the analysis. Hence, we introduce all of these measurements here, together with some context and cautions on their use.

Gaia reports PPPM values (at epoch 2015.5) of (R.A., decl.)_{J2000} = (17:58:46.4171136073, −27:37:04.543560775) \pm (0.16, 0.14) mas,

$$\pi_G = 0.73 \pm 0.18 \text{ mas}, \quad (9)$$

and

$$\boldsymbol{\mu}_G(N, E) = (-1.24 \pm 0.26, -1.58 \pm 0.31) \text{ mas yr}^{-1}. \quad (10)$$

Gaia also reports all 10 correlation coefficients, but the only one of interest for our purposes is the one associated with the last equation, 0.31. Before continuing, we note that Gaia parallaxes have a color-dependent zero-point error. For relatively red stars (due to intrinsic color or reddening), the shift is measured to be $\pi_{\text{shift}} = 0.055 \text{ mas}$ (Zinn et al. 2019). Hence, we correct the baseline object parallax to be

$$\pi_{\text{base}} = 0.78 \pm 0.18 \text{ mas}. \quad (11)$$

While the Gaia PPPM catalog is by far the best large-scale astrometric database ever constructed, its performance in the crowded fields of the Galactic bulge is not at the same level as in high-latitude fields, or even as in the other parts of the Galactic plane. For example, Hirao et al. (2020) found that the Gaia proper-motion measurement of the baseline object of OGLE-2017-BLG-0406 was spurious. This itself shows that Gaia measurements in crowded fields must be treated with caution.

However, Hirao et al. (2020) also showed, based on generally more precise (and, likely, more accurate) OGLE proper motions of stars in the same field, that the reported Gaia proper motions of most stars are very reliable. In particular, after Hirao et al. (2020) eliminated stars with $\sigma(\pi)/\pi < -2$ (which included OGLE-2017-BLG-0406S itself) and $\sigma(\mu_{\text{north}}) > 0.6$ or $\sigma(\mu_{\text{east}}) > 0.6 \text{ mas yr}^{-1}$, only 1%–2% of Gaia proper motions were $>3\sigma$ outliers. However, the Gaia proper-motion errors had to be renormalized by a factor of 2.2 to enforce $\chi^2/\text{dof} = 1$. Although the exact reason for this renormalization is not known, it is likely that bulge field crowding is a major contributing cause. In particular, the Gaia mirror has an axis ratio of 3, meaning that the Gaia point-spread function (PSF) has the same ratio. Hence, as Gaia observes a field at various random orientations, light from faint ambient stars can enter the elongated PSF aperture, leading to random shifts in the astrometric centroid. This can lead to excess noise relative to the photon-based error estimates, and this excess noise is tabulated as the astrometric excess noise sig (AENS) parameter. Insofar as this excess noise is truly random, it just degrades the measurement, which is reflected in the reported uncertainties. However, because it is likely due to real stars, whose positions change very little, and because the observing pattern is also not truly random, this excess noise can lead to systematic errors that are larger than the random errors.

In their study of Gaia proper-motion errors, Hirao et al. (2020) considered stars with AENS < 10 , so their results strictly apply to such stars. They did not notice any trends in behavior with AENS, and (though not specifically reported) they also did not notice any trends for AENS at a few times this level.

For OGLE-2018-BLG-1269, Gaia reports AENS = 10.4. We therefore apply the Hirao et al. (2020) error renormalization to the above Gaia measurements. Although Hirao et al. (2020) only studied proper-motion errors (because this is the only quantity for which OGLE measurements are superior to Gaia), we apply this renormalization to all PPPM quantities.

For the position measurement, the formal errors ($\sim 0.15 \text{ mas}$) are so small that they play no practical role, even after renormalization. So we ignore these errors. For the parallax measurement, the renormalized error is $\sim 45\%$ of the measured value. Hence, its role is mainly qualitative confirmation that the lens is nearby. The renormalized proper-motion errors ($\sim 0.7 \text{ mas yr}^{-1}$) are still relatively small, and this measurement will play a crucial role at several points.

4.3. Blend Is Due to Host and/or Its Companion

4.3.1. Gaia Baseline Object Is $< 20 \text{ mas}$ from Source

Gaia astrometry is generally given for epoch 2015.50, whereas the event peaked at 2018.61. In order to compare the position of the source (at 2018.61) with the position of the Gaia baseline object at the same time, we first propagate the positions of all Gaia stars (including the baseline object) forward in time by $\Delta t = 2018.61 - 2015.50 = 3.11 \text{ yr}$. That is, for each star in the field, i , we calculate

$$\boldsymbol{\theta}_{i,\text{Gaia}}^{2018.61} = \boldsymbol{\theta}_{i,\text{Gaia}}^{2015.5} + \boldsymbol{\mu}_{i,\text{Gaia}} \Delta t, \quad (12)$$

where $\boldsymbol{\mu}_{i,\text{Gaia}}$ is the proper motion of the Gaia object. We then cross-match the Gaia and KMTNet pyDIA catalogs within a $2'$ square, excluding entries that fail a relatively forgiving cut on an empirical $(G - I)/(V - I)$ color–color relation and with a

³² By contrast, Gaia parallax measurements of microlens sources, which are nearly all in the bulge, are of no practical use.

1'' astrometric cut (to allow for optical distortion of the KMTNet camera). Next, we fit for a transformation from Gaia to KMTNet pyDIA coordinates using all matches obtained from the previous step, except the baseline object, by minimizing the unrenormalized χ^2 ,

$$\chi^2 = \sum_i [\theta_{i,\text{KMTNet}}^{2018.61} - T_n(\theta_{i,\text{Gaia}}^{2018.61})]^2, \quad (13)$$

where T_n is a n th-order polynomial transformation, i.e., 6, 12, and 20 parameters for $n = (1, 2, 3)$.

We find that the results vary very little, but the $n = 3$ polynomial fit is slightly better than the others. We recursively eliminate outliers, of which there are 46 objects³³ for 487 original matches. The scatter is 19 mas, which is almost an order of magnitude larger than the typical formal propagated errors in $\theta_{i,\text{Gaia}}^{2018.61}$. Although the Gaia errors are probably somewhat underestimated in crowded fields (Hirao et al. 2020), it is still the case that this scatter is completely dominated by the errors of KMTNet pyDIA astrometry.

We then apply the resulting transformation to the propagated Gaia blend position $\theta_{b,\text{Gaia}}^{2018.61}$ and subtract this from the pyDIA source position that is derived from difference images:

$$\begin{aligned} \Delta\theta(N, E) &= \theta_{S,\text{KMTNet}}^{2018.61} - T_3(\theta_{b,\text{Gaia}}^{2018.61}) \\ &= (6.9, 9.2) \pm (4.4, 4.4) \text{ mas}. \end{aligned} \quad (14)$$

The error comes from three sources added in quadrature: error in the transformation coefficients (1.0 mas), error in the propagated value of $\theta_{b,\text{Gaia}}^{2018.61}$ (2.0 mas), and error in the pyDIA measurement of $\theta_{S,\text{KMTNet}}^{2018.61}$ (4.0 mas).

That is, the Gaia baseline object lies 11.5 ± 4.4 mas from the source at the time of the event. We repeat this exercise using OGLE data and obtain 18.5 ± 4.4 mas, which confirms that the source and the Gaia baseline object are very close.

4.3.2. Probability of Chance Superposition Is $p = 3 \times 10^{-6}$

Figure 5 shows that the blend is bright and belongs to the foreground main-sequence branch, i.e., $(V - I, I)_b = (1.79 \pm 0.02, 15.80 \pm 0.01)$. The surface density of such bright ($I < 16$), blue ($V - I < 2$) foreground stars is only $n = 9 \text{ arcmin}^{-2}$. In the previous subsection, we showed that the Gaia baseline object is within $\delta\theta = 20$ mas. Therefore, the probability of an unrelated bright foreground star lying within $\delta\theta$ of this foreground star lens is $\pi(\delta\theta)^2 n = 3 \times 10^{-6}$. Hence, the blend is almost certainly associated with the event, rather than being a random interloper.

4.3.3. Blended Light Is Due to the Lens System

There are five broad classes of objects that could contribute significantly to the baseline object: (1) the source, (2) a stellar companion to the source, (3) the lens host, (4) a stellar companion to the host, and (5) an unrelated ambient star.

Of course, the source does contribute, but this contribution is well determined from the microlensing fit, and in the present case, it is also quite small. The remaining four possibilities are candidates for the remaining light, i.e., the blend. The $p = 3 \times 10^{-6}$ probability just calculated implies that class

(5) is ruled out. Moreover, class (2) is also ruled out by the color (1 mag bluer than the clump) and magnitude (0.5 mag brighter than the clump). To be a companion of the source (and hence in the bulge), this would have to be a late B dwarf, of which there are essentially none in the bulge (apart from the star-forming regions near the Galactic center).

Thus, the blended light is due to either the host, a companion to the host, or possibly a combination of the two. For any of these possibilities, the parallax and proper motion of the host are essentially equal to the parallax and proper motion of the blend because the host and its putative companion are at essentially the same distance, and their orbital motion is very slow compared the lens–source relative motion. Hence, the Gaia measurements of these quantities will act as strong constraints on the estimates of the physical parameters of the lens system.

4.4. Bayesian Analysis

For the Bayesian analysis, we will incorporate the Gaia astrometric measurements in addition to the usual microlensing-parameter measurements.

4.4.1. Inputs from Gaia

To do so, we first note that for the three parameters $\mathbf{X} = (\pi, \boldsymbol{\mu})$ measured by Gaia, the observed (baseline object) quantities are related to the underlying physical (source and lens) quantities³⁴ by (Ryu et al. 2019)

$$\mathbf{X}_{\text{base}} = (1 - \eta)\mathbf{X}_L + \eta\mathbf{X}_S, \quad (15)$$

where $\eta = f_S/f_{\text{base}}$ is the flux fraction of the source in the Gaia band and (f_S, f_{base}) are the flux of the source and the baseline object, respectively. We estimate η by noting that the peak of the Gaia passband is broadly consistent with that of the V band, and the typical photometric error of the Gaia observation is 2%. We thereby estimate $\eta = 0.02$ based on our result that the blend is 4.2 mag brighter than the source in the V band.

To find the lens parallax π_L , we adopt $\pi_S = 0.13 \pm 0.01$ mas from Nataf et al. (2013), and we renormalize the errors (by a factor 2.2) in Equation (11) to obtain $\pi_{\text{base}} = 0.78 \pm 0.40$ mas. We then apply Equation (15) to π_{base} and find

$$\pi_L = 0.80 \pm 0.40 \text{ mas}. \quad (16)$$

The situation is substantially more complicated for the proper motion. First, the microlensing solution gives the amplitude of the lens–source relative proper motion in the geocentric frame, but the Gaia proper motion is in the heliocentric frame. We can relate these by

$$\begin{aligned} \boldsymbol{\mu}_{\text{rel, hel}} &\equiv \boldsymbol{\mu}_{L, \text{hel}} - \boldsymbol{\mu}_{S, \text{hel}}; \\ \times \boldsymbol{\mu}_{\text{rel, hel}} &= \boldsymbol{\mu}_{\text{rel}} + \frac{\pi_{\text{rel}}}{\text{au}} \boldsymbol{\nu}_{\oplus, \perp}, \end{aligned} \quad (17)$$

where $\boldsymbol{\nu}_{\oplus, \perp}(N, E) = (-1.7, 18.4) \text{ km s}^{-1}$ is the projected velocity of Earth at t_0 and $(\boldsymbol{\mu}_{L, \text{hel}}, \boldsymbol{\mu}_{S, \text{hel}})$ are the heliocentric proper motions of the lens and source, respectively.

In principle, we could fully incorporate Equations (15) and (17) into the Bayesian analysis below. However, as we now

³³ We note that roughly half are false matches due to the relatively loose matching criteria, and the remainder are likely due to corrupted astrometry from unresolved objects.

³⁴ In the more general case, one would write “source” and “blend.” However, in Section 4.3.3, we established that the blend is the lens (although up to this point, it is not yet clear whether it can be identified with the host, its stellar companion, or both).

show, for the case of OGLE-2018-BLG-1269, the lens proper motion is well approximated by $\boldsymbol{\mu}_{L,\text{hel}} = \boldsymbol{\mu}_{\text{base}}$.

First, we combine Equations (15) and (17) to yield

$$\begin{aligned}\boldsymbol{\mu}_{L,\text{hel}} &= \boldsymbol{\mu}_{\text{base}} + \eta[\boldsymbol{\mu}_{\text{rel}} + \frac{\pi_{\text{rel}}}{\text{au}}\boldsymbol{\nu}_{\oplus,\perp}], \\ \boldsymbol{\mu}_{S,\text{hel}} &= \boldsymbol{\mu}_{\text{base}} - (1 - \eta)[\boldsymbol{\mu}_{\text{rel}} + \frac{\pi_{\text{rel}}}{\text{au}}\boldsymbol{\nu}_{\oplus,\perp}].\end{aligned}\quad (18)$$

Next, we note that for typical final values of $\pi_{\text{rel}} = 0.4$ mas, we have $(\pi_{\text{rel}}/\text{au})\boldsymbol{\nu}_{\oplus,\perp} \simeq 1.6 \text{ mas yr}^{-1} \ll \boldsymbol{\mu}_{\text{rel}}$; hence, regardless of the direction of $\boldsymbol{\mu}_{\text{rel}}$, we have $\boldsymbol{\mu}_{\text{rel, hel}} \simeq \boldsymbol{\mu}_{\text{rel}} \simeq 8 \text{ mas yr}^{-1}$. Therefore, the second term in the first entry of Equation (18) is of order $\eta\boldsymbol{\mu}_{\text{rel}} \sim 0.16 \text{ mas yr}^{-1}$, which is a factor of about 4 smaller than the renormalized errors in $\boldsymbol{\mu}_{\text{base}}$ ($\sim 0.7 \text{ mas yr}^{-1}$). Hence, we adopt $\boldsymbol{\mu}_{L,\text{hel}} = \boldsymbol{\mu}_{\text{base}}$. Then, after renormalizing the errors (by a factor of 2.2) in Equation (10) and rotating to Galactic coordinates, we obtain

$$\boldsymbol{\mu}_L(l, b) = (-1.86 \pm 0.68, 0.75 \pm 0.57) \text{ mas yr}^{-1}. \quad (19)$$

4.4.2. Bayesian Formalism

With the four measured constraints $(t_E, \theta_E, \pi_L, \pi_E)$, we now make a Bayesian analysis following the procedure of Jung et al. (2018). We first build a Galactic model with models of the mass function (MF), density profile (DP), and velocity distribution (VD) of astronomical objects. For the MF and DP, we adopt the models used in Jung et al. (2018). For the VD, we use the proper-motion distribution of stars measured by Gaia. For the source proper motion, we examine a Gaia CMD using red giant stars within $3'$ centered on the event direction and find their mean proper motion and standard deviation in Galactic coordinates:

$$\boldsymbol{\mu}_S(l, b) = (-5.93 \pm 3.10, 0.03 \pm 2.72) \text{ mas yr}^{-1}. \quad (20)$$

For the lens proper motion, we employ Equation (19).

For each solution of $u_0 > 0$ and $u_0 < 0$, we draw 1 billion random events based on the adopted Galactic model. For each random event i , we then infer the four parameters $(t_E, \theta_E, \pi_L, \pi_E)_i$ and find the χ^2 difference between the inferred and measured values, i.e.,

$$\begin{aligned}\chi_{\text{gal},i}^2 &= \chi_i^2(t_E) + \chi_i^2(\theta_E) + \chi_i^2(\pi_L) + \chi_{p,i}^2; \\ \chi_{p,i}^2 &= \sum_j (a_i - a_0)_j c_{jk}^{-1} (a_i - a_0)_k,\end{aligned}\quad (21)$$

where $\mathbf{a}_i = \boldsymbol{\pi}_{E,i} = (\pi_{E,N}, \pi_{E,E})_i$ is the inferred parallax, and \mathbf{a}_0 and c_{jk} are the measured π_E and its covariance matrix, respectively. We next find the likelihood of the event by $P_i = \exp(-\chi_{\text{gal},i}^2/2) \times \Gamma_i$, where $\Gamma_i \propto \theta_{E,i} \mu_{\text{rel},i}$ is the lensing event rate.

For each random event i , we also infer the lens position in the calibrated CMD, i.e., $(V - I, I)_L$, in order to check whether the lens flux predicted from the Bayesian estimates is consistent with the blended flux. For this, we first construct a set of isochrones with different metallicities and ages (Spada et al. 2017), i.e., with $[\text{Fe}/\text{H}] = (-0.5, 0.0, +0.3)$ and age = (2, 4, 6, 8, 10) Gyr. In each isochrone j , we next estimate the absolute I -band magnitude $M_{I,L,i,j}$ and intrinsic $(V - I)_{0,L,i,j}$ color of the lens from the inferred lens mass M_i . We then find the dereddened lens magnitude in the I and V bands by $I_{0,L,i,j} = M_{I,L,i,j} + 5 \log(D_{L,i}/\text{pc}) - 5$ and $V_{0,L,i,j} = I_{0,L,i,j} + (V - I)_{0,L,i,j}$. We

next estimate the extinction to the lens $A_{\lambda,L,i}$ using the partial extinction model (Bennett et al. 2015; Beaulieu et al. 2016),

$$A_{\lambda,L,i} = \frac{1 - e^{-|D_{L,i}/\tau_{\text{dust}}|}}{1 - e^{-|D_{S,i}/\tau_{\text{dust}}|}} A_{\lambda,S}, \quad (22)$$

where the index λ denotes the passband and $\tau_{\text{dust}} = (0.12 \text{ kpc})/\sin(b)$ is the dust scale height. Here $A_{\lambda,S}$ is the extinction to the source, for which we adopt $A_{I,S} = 1.98$ and $E(V - I)_S = 1.76$ from our CMD analysis (Equation (4)). We then derive $(V - I, I)_{L,i,j}$ using $A_{\lambda,L,i}$ and bin the CMD by these lens positions with the likelihood P_i .

We emphasize that in this initial analysis, we completely ignore the constraints coming from the blended light. That is, we neither impose any constraint on the lens light (such as not to exceed the blended light) nor consider the possibility that the lens is responsible for the blended light. At this point, we simply ‘‘predict’’ the lens color and magnitude based on the $(t_E, \theta_E, \pi_L, \pi_E)$ (or (t_E, θ_E, π_L)) constraints, together with the Galactic model and model isochrones. We investigate the role of the blended light in constraining the solution only after comparing these predictions to the observed blended light.

4.4.3. Bayesian Results

We finally investigate the posterior probabilities of the lens properties from all random events. We note that to check the contribution of the π_E constraint on the Bayesian estimates, we also explore the posterior probabilities with (t_E, θ_E, π_L) constraints.

The results from the constraints $(t_E, \theta_E, \pi_L, \pi_E)$ are shown in Figure 6 and listed in Table 2. Also listed are the total Galactic model probability $P_{\text{tot}} = \sum P_i$ and net relative probability $P_{\text{net}} = P_{\text{tot}} P_{1c}$, where $P_{1c} = \exp(-\Delta\chi^2/2)$ is the relative fit probability and $\Delta\chi^2$ is the χ^2 difference between the two solutions. Here $\phi_{\text{hel}} = \tan^{-1}[\mu_{\text{rel, hel}}(E)/\mu_{\text{rel, hel}}(N)]$ is the orientation angle of $\boldsymbol{\mu}_{\text{rel, hel}}$.

We find that the measured π_E from modeling gives a strong constraint on the probability distributions. However, we also find that the host mass ranges of the two solutions ($u_0 > 0$ and $u_0 < 0$) are somewhat different from each other. Because π_E is the only prior constraint that differs significantly between the two solutions and is connected to the lens mass (Equation (2)), the difference would imply that the Galactic model priors disfavor one of the solutions. To check this, we also draw the two-dimensional (2D) likelihood \mathcal{L} for the lens parameters obtained from the (t_E, θ_E, π_L) and $(t_E, \theta_E, \pi_L, \pi_E)$ constraints. See Figure 7. We note that the black and gray error bars in the three $(\pi_{E,N}, \pi_{E,E})$ planes are the errors of π_E listed in Table 1 for the $u_0 > 0$ and $u_0 < 0$ solutions, respectively. From this figure, we find that the measured π_E from both the $u_0 > 0$ and $u_0 < 0$ solutions are consistent at the 1σ level. This mutual consistency is reflected in the almost equal values of P_{tot} (ratio 0.92) in Table 2. Thus, our estimates should reflect the weighted average of the two solutions, although these hardly differ.

Hence, these results, which do not yet incorporate constraints from the blended light, suggest that the host is a Sun-like star with $M_1 = 1.13_{-0.35}^{+0.72} M_{\odot}$ located at a distance of $D_L = 2.56_{-0.62}^{+0.92} \text{ kpc}$. Then, the microlensing companion is a planet with $M_2 = 0.69_{-1.17}^{+0.44} M_J$ separated (in projection) from the host by $a_L = 4.61_{-1.17}^{+1.70} \text{ au}$. That is, the planet is a cold giant lying beyond the snow line, i.e., $a_{sl} = 2.7 \text{ au}(M_1/M_{\odot}) \sim 3.1 \text{ au}$.

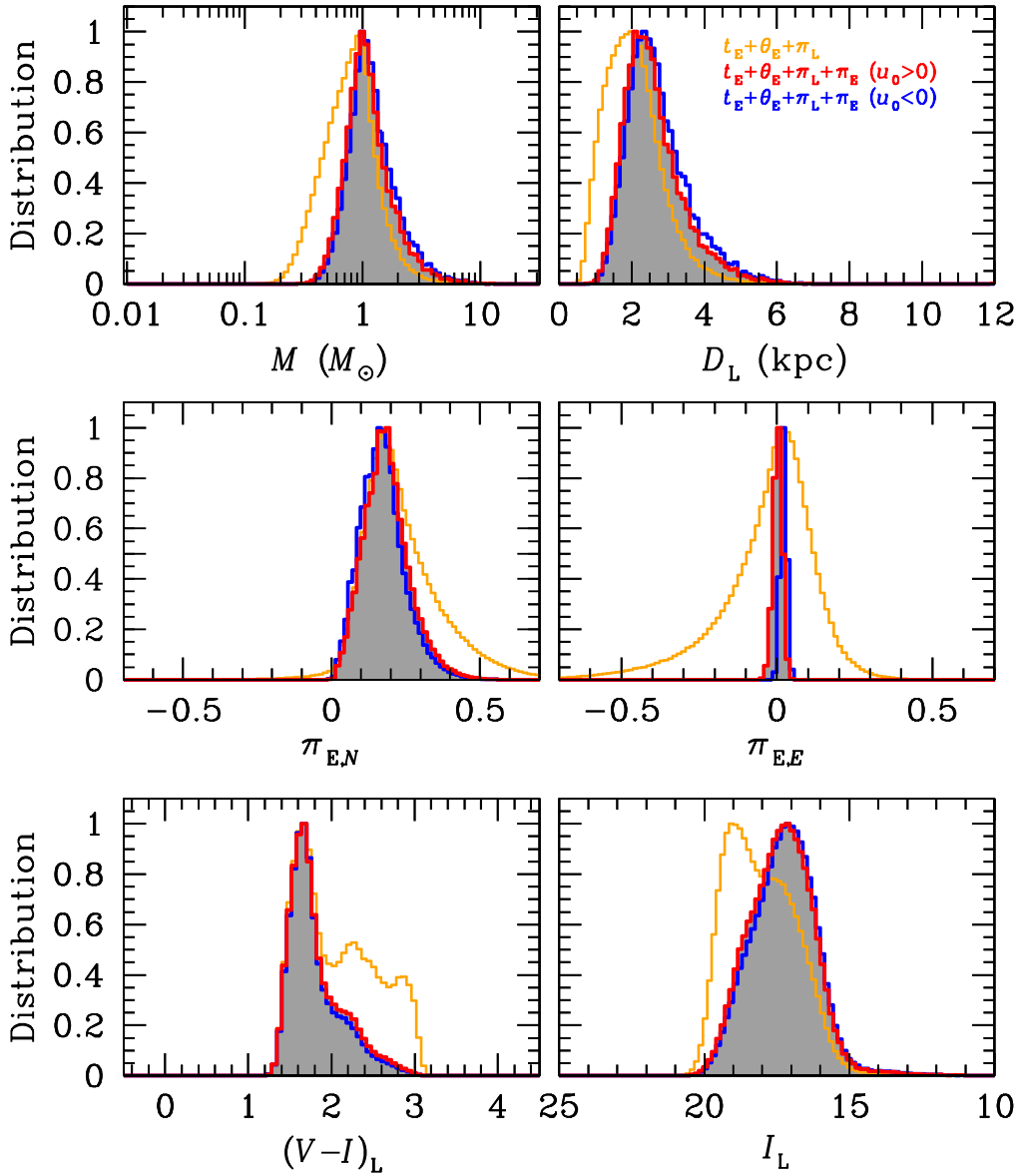


Figure 6. Posterior distributions for the lens parameters. In each panel, the yellow curve shows the distribution obtained from the timescale t_E , angular Einstein radius θ_E , and lens parallax π_L constraints. The red and blue curves are, respectively, the distributions for the $u_0 > 0$ and $u_0 < 0$ solutions derived from t_E , θ_E , and π_L and the microlens parallax π_E constraints.

Table 2
Physical Parameters

Parameters	$u_0 > 0$	$u_0 < 0$	Weighted
$M_1 (M_\odot)$	$1.11^{+0.68}_{-0.34}$	$1.18^{+0.78}_{-0.36}$	$1.13^{+0.72}_{-0.35}$
$M_2 (M_J)$	$0.67^{+0.41}_{-0.21}$	$0.74^{+0.49}_{-0.23}$	$0.69^{+0.44}_{-0.22}$
a_\perp (au)	$4.51^{+1.66}_{-1.15}$	$4.75^{+1.74}_{-1.21}$	$4.61^{+1.70}_{-1.17}$
D_L (kpc)	$2.51^{+0.90}_{-0.61}$	$2.64^{+0.94}_{-0.64}$	$2.56^{+0.92}_{-0.62}$
$\pi_{E,N}$	$0.187^{+0.078}_{-0.071}$	$0.174^{+0.074}_{-0.071}$	$0.183^{+0.077}_{-0.071}$
$\pi_{E,E}$	$0.011^{+0.014}_{-0.017}$	$0.029^{+0.011}_{-0.014}$	$0.018^{+0.014}_{-0.019}$
$\mu_{\text{rel, hel}}(N)$ (mas yr $^{-1}$)	$8.01^{+0.59}_{-0.65}$	$7.91^{+0.63}_{-0.68}$	$7.97^{+0.62}_{-0.66}$
$\mu_{\text{rel, hel}}(E)$ (mas yr $^{-1}$)	$1.56^{+0.57}_{-0.56}$	$2.37^{+0.63}_{-0.56}$	$1.84^{+0.81}_{-0.68}$
ϕ_{hel} (deg)	$11.02^{+2.89}_{-3.28}$	$16.68^{+2.68}_{-2.63}$	$13.00^{+4.14}_{-3.98}$
$(V-I)_L$	$1.76^{+0.44}_{-0.20}$	$1.74^{+0.41}_{-0.19}$	$1.75^{+0.44}_{-0.20}$
I_L	$17.40^{+1.15}_{-1.06}$	$17.30^{+1.15}_{-1.03}$	$17.36^{+1.16}_{-1.04}$
P_{lc}	1.0	0.64	...
P_{tot}	416,913.4	382,315.5	...
P_{net}	416,913.4	244,681.9	...

It is of some interest to understand how the Bayesian analysis constrains the lens mass to a range of a factor of ~ 2.4 at the 1σ level despite the fact that π_E varies by a factor of 10 at 1σ (see Figure 4), while $M = \theta_E / \kappa \pi_E$. The main reason is that the direction of μ_{rel} (and so the direction of π_E) is reasonably well constrained by the Gaia measurement of μ_L , together with the relatively large value of $\mu_{\text{rel}} \simeq 8.3$ mas yr $^{-1}$. This is illustrated in Figure 8, which shows μ_L and a blue circle to represent all possible μ_S values that are consistent with $\mu_{\text{rel}} = |\mu_L - \mu_S|$. The magenta arc of this circle represents the 1σ range of μ_S as given by Equation (20). The arc of allowed (at 1σ) directions is shown by dashed lines. This same arc, rotated to equatorial coordinates (and displayed as lens–source rather than source–lens motion), is shown in Figure 4, with boundaries $\phi = 16^\circ$ – 43° (north through east). The first point to note is that, for both $u_0 > 0$ and $u_0 < 0$, this arc subtends a region that is almost entirely contained within the 1σ π_E contours, implying mutual consistency between two

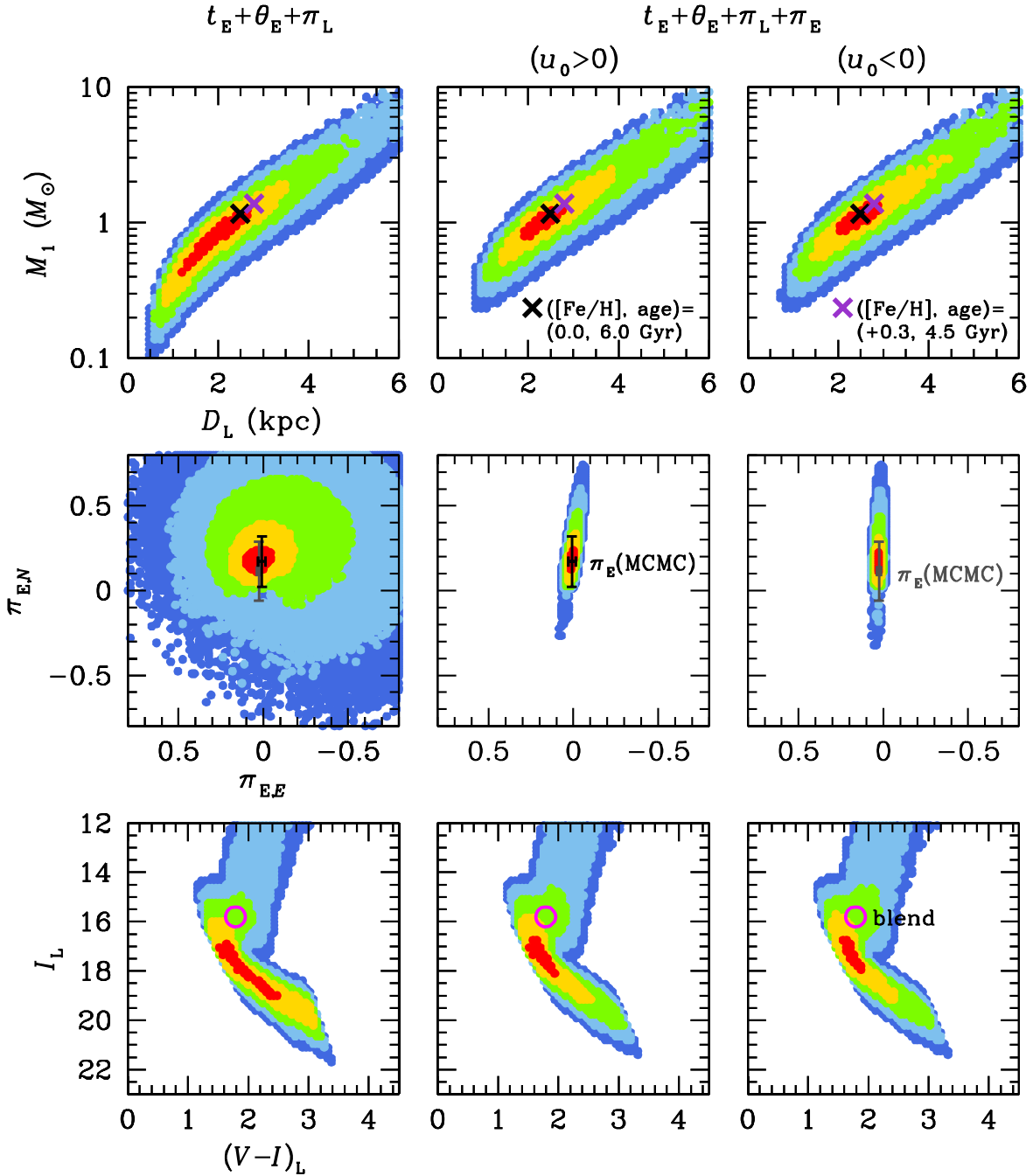


Figure 7. The $-\Delta \ln \mathcal{L}$ contours in the (M_1, D_L) , $(\pi_{E,N}, \pi_{E,E})$, and $(V-I, I_L)$ planes. The left panels show the contours from (t_E, θ_E, π_L) constraints. The middle and right panels show the contours for the $u_0 > 0$ and $u_0 < 0$ solutions from $(t_E, \theta_E, \pi_L, \pi_E)$ constraints. The black and gray error bars represent the errors of π_E listed in Table 1 for the $u_0 > 0$ and $u_0 < 0$ solutions, respectively. The magenta circles are the location of the blended light measured from the CMD analysis (see Figure 5). The black and purple crosses are the blend positions estimated by matching the observed isochrones to the blended light for the $[\text{Fe}/\text{H}] = 0.0$ and $+0.3$ isochrones, respectively (see Figure 9). The color notation is identical to that of Figure 4.

constraints on the direction that are entirely independent. Second, for the $u_0 < 0$ contours, which are almost perfectly vertical, we can evaluate the range of π_E as $\pi_E(16^\circ)/\pi_E(43^\circ) = \csc(16^\circ)/\csc(43^\circ) = 2.47$. This confirms that the relatively tight constraints on M in the Bayesian analysis derive from the application of the directional constraint on lens–source relative motion (Figure 8) to the 1D parallax contours from the light-curve analysis (Figure 4). That is, the Bayesian mass estimate comes primarily from a combination of measured microlensing parameters and lens proper motion, while the

Galactic model enters mainly by constraints on the source proper motion.

5. Blended Light Is Due Mainly to the Host

As we discussed in Section 4, the facts that the lens host is known (from the Bayesian analysis) to be a roughly solar-mass foreground disk star and that there is such a roughly solar-mass foreground disk star projected within ~ 12 mas of the lens make it virtually certain that this blended light comes from the lens system. That is, the blended light must be due to the host, a

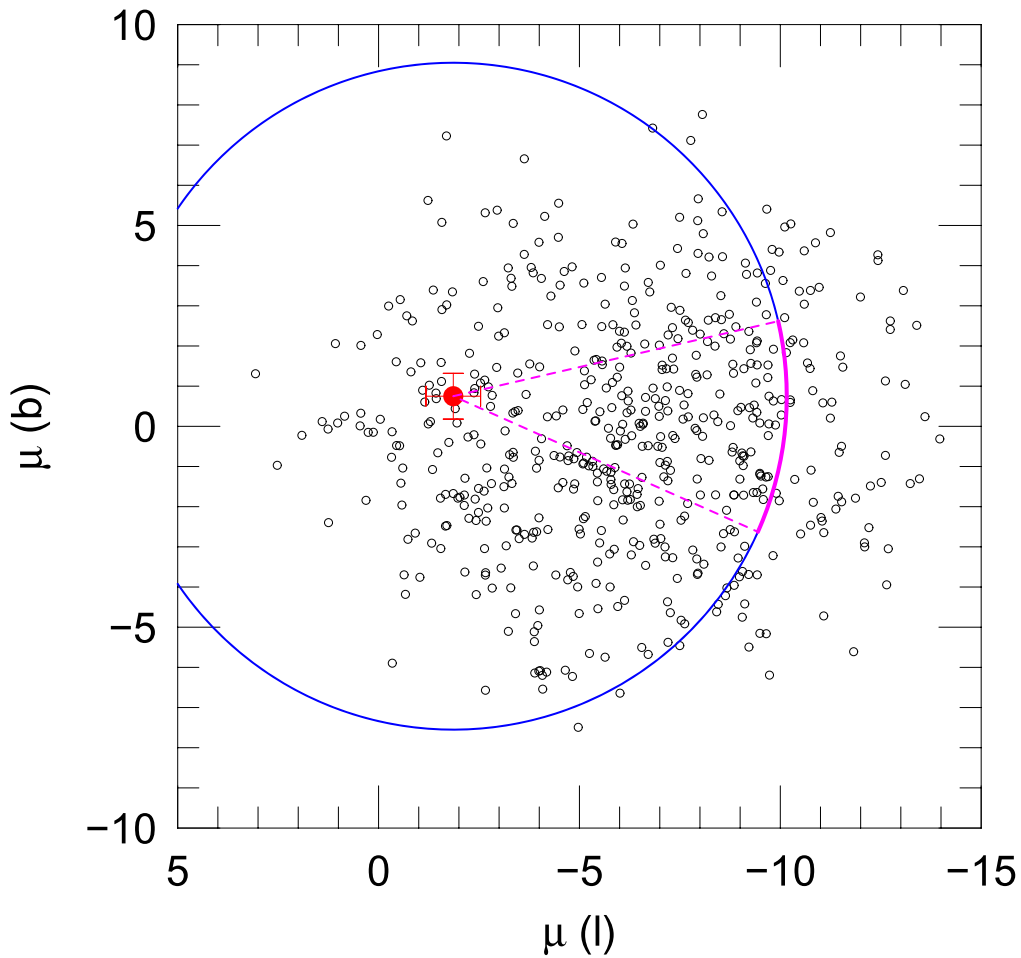


Figure 8. The proper motion of the lens (red) is shown relative to those of bulge clump giant stars (black) within a $3'$ circle centered on OGLE-2018-BLG-1269, which is a tracer of the general population of bulge sources. The blue circle is the locus of possible source proper motions, given that $\mu_{\text{rel}} = |\mu_{\text{L}} - \mu_{\text{S}}| = 8.3 \pm 0.6 \text{ mas yr}^{-1}$. The magenta arc is the portion of this circle that is consistent at the 1σ level with the proper-motion distribution of bulge sources in the b direction. When this arc is projected onto the microlens contours (Figure 4), it strongly constrains the parallax along the long direction of those contours.

companion to the host, or some combination of the two (Koshimoto et al. 2020). Here we examine this issue in detail.

The two lower right panels of Figure 7 show that the blend (magenta circle) lies at about 2.5σ from the most likely prediction of the Bayesian analysis for both the $u_0 > 0$ and $u_0 < 0$ solutions. However, this nominal 2.5σ discrepancy may simply reflect the fact that stars spend far more time on the upper main sequence than they do at the location of the blend (i.e., the subgiant branch, or possibly the end of the turnoff). That is, a small range of lens masses from the upper main sequence are projected onto a small region of the CMD, but an equally small range of masses that are just slightly larger are projected all across the subgiant branch and thus populate the CMD at much lower density. Hence, the blended light could be fully consistent with being due to the host but would show up as “relatively low probability” on this figure.

We now must take account of the fact that, despite the low prior probability that the host is a turnoff/subgiant star (as indicated by it being projected against the green contours in Figure 7), there is actually such a star associated with the event, i.e., either the host itself, a companion to the host, or a combination of the two. We now consider these three possibilities in turn.

5.1. Blend Is Consistent with Being Due to the Host

We first ask whether the host is consistent with being the primary contributor to the blended light. If it is, then there must be a star simultaneously consistent with the microlensing properties and the blended light. For this analysis, we use the measured Einstein radius θ_{E} and the adopted source parallax π_{S} (Equation (2)) to map a set of model isochrones to the calibrated CMD. Given θ_{E} and π_{S} , we can take a star with given mass M_{iso} , intrinsic color $(V - I)_{0,\text{iso}}$, and absolute magnitude $M_{I,\text{iso}}$ to estimate the distance to the star D_{iso} . We next find the dereddened I - and V -band magnitudes by $I_{0,\text{iso}} = M_{I,\text{iso}} + 5 \log(D_{\text{iso}}/\text{pc}) - 5$ and $V_{0,\text{iso}} = I_{0,\text{iso}} + (V - I)_{0,\text{iso}}$. We then find the position of the star $(V - I, I)_{\text{iso}}$ in the calibrated CMD using the partial extinction model (Equation (22)). Finally, we build an observed isochrone with $[M, D, (V - I), I]_{\text{iso}}$ from all stars listed in the model isochrone. For the three cases of $[\text{Fe}/\text{H}] = (-0.5, 0.0, +0.3)$, we then construct observed isochrones with different ages and compare them to the blended light to estimate the blend mass M_{b} and distance D_{b} .

We find that two observed isochrones can match the blended light (see Figure 9). That is, the two curves for $([\text{Fe}/\text{H}], \text{age}) = (0.0, 6 \text{ Gyr})$ and $(+0.3, 4.5 \text{ Gyr})$ pass through the blend position with an offset of $(5.5, 8.5) \times 10^{-3}$, respectively. The estimated

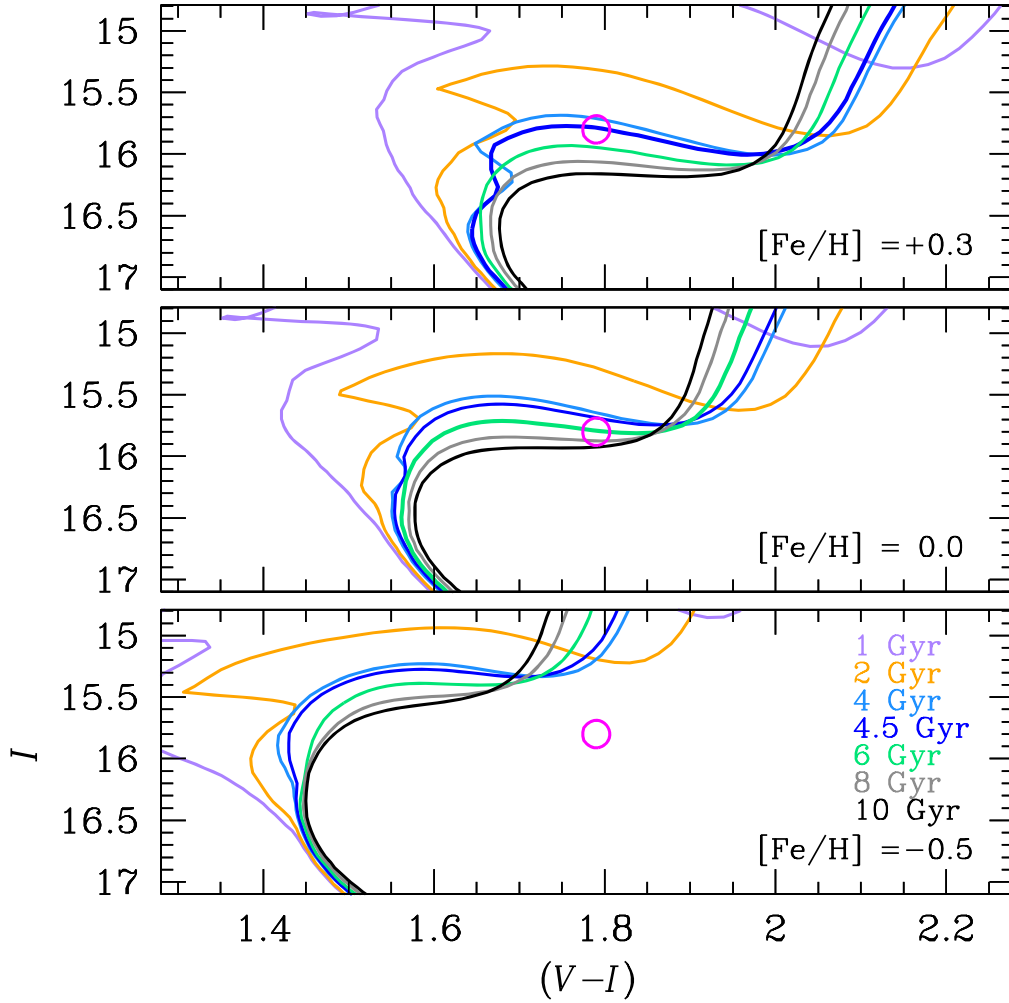


Figure 9. Model isochrones calibrated to the observed CMD. In each panel, the curves with different colors are the observed isochrones from different metallicities and ages. The magenta circle is the position of the blended light. The green curve (6 Gyr) in the middle panel ($[\text{Fe}/\text{H}] = 0.0$) and the blue curve (4.5 Gyr) in the upper panel ($[\text{Fe}/\text{H}] = +0.3$) are the two isochrones that pass over the observed color and magnitude of the blended light.

mass and distance to the blend are $(M_b, D_b) = (1.16 M_\odot, 2.49 \text{ kpc})$ for $([\text{Fe}/\text{H}], \text{age}) = (0.0, 6 \text{ Gyr})$ and $(M_b, D_b) = (1.38 M_\odot, 2.80 \text{ kpc})$ for $([\text{Fe}/\text{H}], \text{age}) = (+0.3, 4.5 \text{ Gyr})$. These estimates imply that for typical disk populations with $0 \leq [\text{Fe}/\text{H}] \leq 0.3$, M_b and D_b are in the range of $1.16 \leq M_b/M_\odot \leq 1.38$ and $2.49 \leq D_b/\text{kpc} \leq 2.80$, respectively. These ranges show remarkable agreement with the prediction from the Bayesian analysis (see Figure 7). This implies that the host is consistent with causing the blended light, which is then a subgiant (or possibly late-turnoff) star.

5.2. Blend as Stellar Companion to the Host (Qualitative Analysis)

We still must consider the possibility that the blended light is primarily due to a stellar companion to the host, rather than the host itself. That is, it is due to a star that does not directly enter into the microlensing event but is gravitationally bound to the host. This alternative explanation for the blended light can be conceptually divided into two cases: either the host contributes very little light to the blend, or the host and its brighter stellar companion both contribute significantly to the observed blended light. When we quantitatively evaluate the probability that the host dominates the blended light, we will treat these two alternative cases as a single case. However, in the

qualitative treatment that follows immediately below, we make a conceptual distinction between them.

In order to evaluate the three possibilities, i.e., that the blend light

1. is dominated by host,
2. is dominated by a stellar companion to the host (and the host contributes relatively little light), and
3. receives comparable contributions from the host and a stellar companion,

we first divide all single and binary systems containing a subgiant (or possibly late-turnoff) star into six classes:

- (A) single stars,
- (B) binaries with orbital periods $P < 10^4$ days,
- (C) binaries with orbital periods $P > 10^{5.3}$ days,
- (D) binaries with $10^4 < P/\text{day} < 10^{5.3}$ and mass ratios $Q < 0.5$,
- (E) binaries with $10^4 < P/\text{day} < 10^{5.3}$ and $0.5 < Q < 0.9$, and
- (F) binaries with $10^4 < P/\text{day} < 10^{5.3}$ and $0.9 < Q < 1$.

Using the statistics of Duquennoy & Mayor (1991) for solar-type stars, we estimate relative fractions (0.36, 0.20, 0.28, 0.10, 0.05, 0.01) for classes (A, B, C, D, E, F), respectively.

These six classes of systems can contribute to the three cases of events as follows. Class (A) can contribute only to the events of case (1). Class (B) cannot contribute to any events with an OGLE-208-BLG-1269–type light curve because companions in this period range would have given rise to recognizable signals in the light curve ($P < 10^4$ days) or would violate the Gaia-based source–blend separation measurement ($P < 10^{5.3}$ days).

Class (C) is excluded for cases (2) and (3) because the centroid of light would be displaced from the lens host by more than 12 mas. However, it is permitted for case (1) because the light from the companion would not significantly displace the light centroid.

Class (D) can contribute to the events of case (1) but not cases (2) or (3). That is, the light contributed by the stellar companion would not be enough to qualitatively alter the photometric appearance of the combined light relative to an isolated turnoff/subgiant star, so case (1) is compatible. However, the mass of the host for case (2) is too low to be compatible with microlensing constraints (see Table 2). Therefore, case (2) is excluded. And case (3) is also excluded because a $Q < 0.5$ companion cannot contribute significantly.

Class (E) can contribute to either case (1) or case (2). Because the two stars in the lens system must be on the same isochrone, in the class (E) mass-ratio range, the more massive star must be above the turnoff, and the less massive one must be below the turnoff. Hence, they differ by at least 1 mag, which implies that they contribute substantially differently to the total light of the blend. From the lower right panels of Figure 7, it is clear that over most of this mass-ratio range, the lower-mass star would have a similar color to the blend. Hence, the brightness of the higher-mass star would be reduced by ~ 0.1 – 0.5 mag, while its color would hardly be altered relative to the blend. Thus, its position on the CMD would be essentially the same as that of the blend. In particular, it would be projected against the same green contours and, in fact, slightly closer to the yellow contours.

Because class (F) systems can contribute only to case (3), we can now qualitatively evaluate the relative likelihood of case (1) (blended light from the turnoff/subgiant star is dominated by the host, i.e., classes (A), (C), and (D) and part of class (E)) and case (2) (blended light from the turnoff/subgiant star is dominated by a companion to the host, i.e., part of class (E)). Then we will return to case (3).

For class (E), in which there are two stars in the system, i.e., higher- and lower-mass stars, the overall probability of lensing is higher than for a single star by $\sqrt{1+Q}$ because there are two well-separated lenses that could give rise to the event. And the relative probability of the lower-mass star giving rise to the event is \sqrt{Q} . Therefore, relative to the single-host case, the absolute lensing probabilities of two stars scale as 1 and \sqrt{Q} , respectively. We can then approximate the lower-mass events of class (E) by $\sqrt{Q} \sim \sqrt{0.7} \sim 0.84$. Then, the probability for case (2) relative to case (1) can be directly evaluated: $p_2/p_1 = (0.05 \times 0.84)/(0.36 + 0.28 + 0.10 + 0.05) = 0.05$.

Naively, event case (3) appears highly disfavored because only system class (F) contributes to it, and this comprises only 1% of all systems. In fact, however, this case requires close examination for proper evaluation.

We first consider the very special subcase that the host and its companion are identical. Then, their colors would be the same as the blend, but their magnitudes would be 0.75 mag

fainter than the blend. In principle, this might have put them on the main sequence. In this case, the low relative probability of such binary systems (1%) would have been counterbalanced by the fact that main-sequence stars are far more common than turnoff/subgiants of the same color. In fact, however, Figure 9 shows that this position (0.75 mag below the blend) is not inhabited by the observed isochrones that we have displayed.

If we consider the broader case of approximately (rather than exactly) equal masses for the two components ($Q \sim 0.9$), we see that essentially the same (above) argument applies to the case. The less massive star will be fainter and bluer than the blend, while the more massive star will be fainter and redder. The upper panel of Figure 9 shows that at $[\text{Fe}/\text{H}] = +0.3$, it is possible for a star to exist on, e.g., the 10 Gyr isochrone that is 0.3 mag fainter and somewhat redder than the blend. However, this position invalidates the main advantage of event cases that was just mentioned above: the lens (or its companion) remains a subgiant and is not on the more populous main sequence. Hence, the probability of this solution is very low. Using the same procedure as above, we derive $p_3/p_1 = (0.01 \times 1.9)/(0.36 + 0.28 + 0.10 + 0.05) = 0.02$.

5.3. Blend as Lens Companion (Quantitative Analysis)

We now conduct a quantitative analysis aimed at both testing the qualitative ideas presented above and deriving a more precise quantitative result. Our starting point is to draw random events from the same Galactic model used for the Bayesian analysis described above and weight each event by the same $(t_E, \theta_E, \pi_L, \pi_E)$ priors. However, for each simulated event, we either accept or reject it according to whether the combined light from the host and some companion drawn from the same isochrone is compatible with the blended light. That is, each simulated event has a corresponding I -band magnitude and $V-I$ color; if there exists a companion along the same isochrone for which the combined light is compatible with the blend, the event is accepted. The entire isochrone is reddened in the same manner as was done for the case where the blend is dominated by the host light. We consider the same $(3 \times 5 = 15)$ isochrones that were analyzed for the host = blend case, i.e., case (1). We note that after investigating these separate-isochrone cases, we must still combine them to obtain an overall relative probability of case (1) versus cases (2) + (3). This step will also require incorporating information about binary frequency.

Figure 10 shows separate 1σ , 2σ , and 3σ contours in the lens mass–distance plane for all accepted+rejected (black, dark gray, light gray) and accepted-only (red, yellow, green) simulated events. We first focus on the five $[\text{Fe}/\text{H}] = -0.5$ isochrones. These show that the accepted contours lie well away from the contours for all trials in each of the panels. This implies that a very small fraction are accepted. Numerically, we find that the 6, 8, and 10 Gyr isochrones have the highest rate of acceptance: about 0.2% for each (see Table 3). To the extent that these do not overlap (which is partial), they would add constructively. Thus, these three isochrones contribute about 0.6%. The other two isochrones contribute negligibly.

We next focus on the $[\text{Fe}/\text{H}] = +0.3$ isochrones. Again, the oldest three isochrones contribute the most. However, such old, very metal-rich stars are very rare within a few kpc of the Sun. Hence, we ignore these. The two youngest isochrones together contribute $< 1\%$.

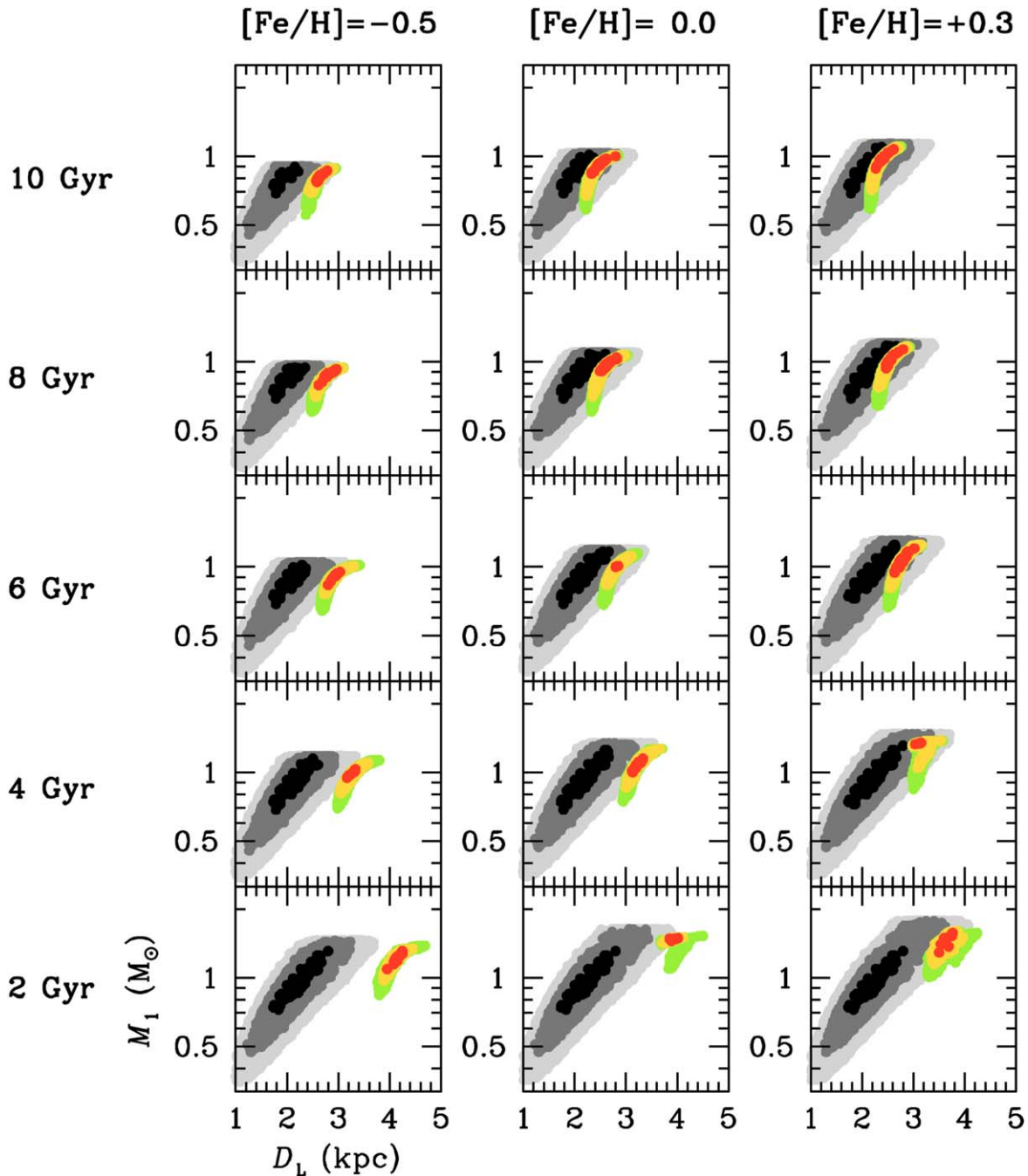


Figure 10. The $-2\Delta\ln\mathcal{L}$ contours in the (M_1, D_L) plane for the accepted+rejected and accepted-only simulated events based on 15 model isochrones, i.e., $[\text{Fe}/\text{H}] = (-0.5, 0.0, +0.3)$ and age = (2, 4, 6, 8, 10) Gyr. In each panel, the black, dark gray, and light gray regions are the 1σ , 2σ , and 3σ contours from both accepted and rejected events. The red, yellow, and green regions are the 1σ , 2σ , and 3σ contours from accepted events.

Table 3
Rate of Acceptance

Age (Gyr)	$[\text{Fe}/\text{H}] = -0.5$	$[\text{Fe}/\text{H}] = 0.0$	$[\text{Fe}/\text{H}] = +0.3$
2	3.56×10^{-6}	1.15×10^{-4}	2.17×10^{-3}
4	4.32×10^{-4}	1.86×10^{-3}	5.97×10^{-3}
6	1.67×10^{-3}	1.43×10^{-2}	2.71×10^{-2}
8	2.24×10^{-3}	2.97×10^{-2}	5.69×10^{-2}
10	2.37×10^{-3}	3.72×10^{-2}	8.19×10^{-2}

Lastly, we examine the solar-metallicity isochrones. These contribute 1.4%, 3.0%, and 3.7% for the 6, 8, and 10 Gyr isochrones, respectively. However, 10 Gyr solar-metallicity

stars are extremely rare, and 8 Gyr solar-metallicity stars are fairly rare, so we make an overall estimate of 3% for solar-metallicity stars. We note that the two youngest isochrones contribute negligibly.

Next, we examine Figure 11, which shows where hosts (red, yellow, green) and stellar companions (black, magenta, cyan) lie on the theoretical isochrones for all 15 isochrone cases. We note that only accepted events are shown. The most important feature of these diagrams is that the stellar companion tracks are almost all confined to the subgiant branch. This confirms the basic logic of the approach that we outlined in the enumeration in Section 5.2, i.e., of considering the relative

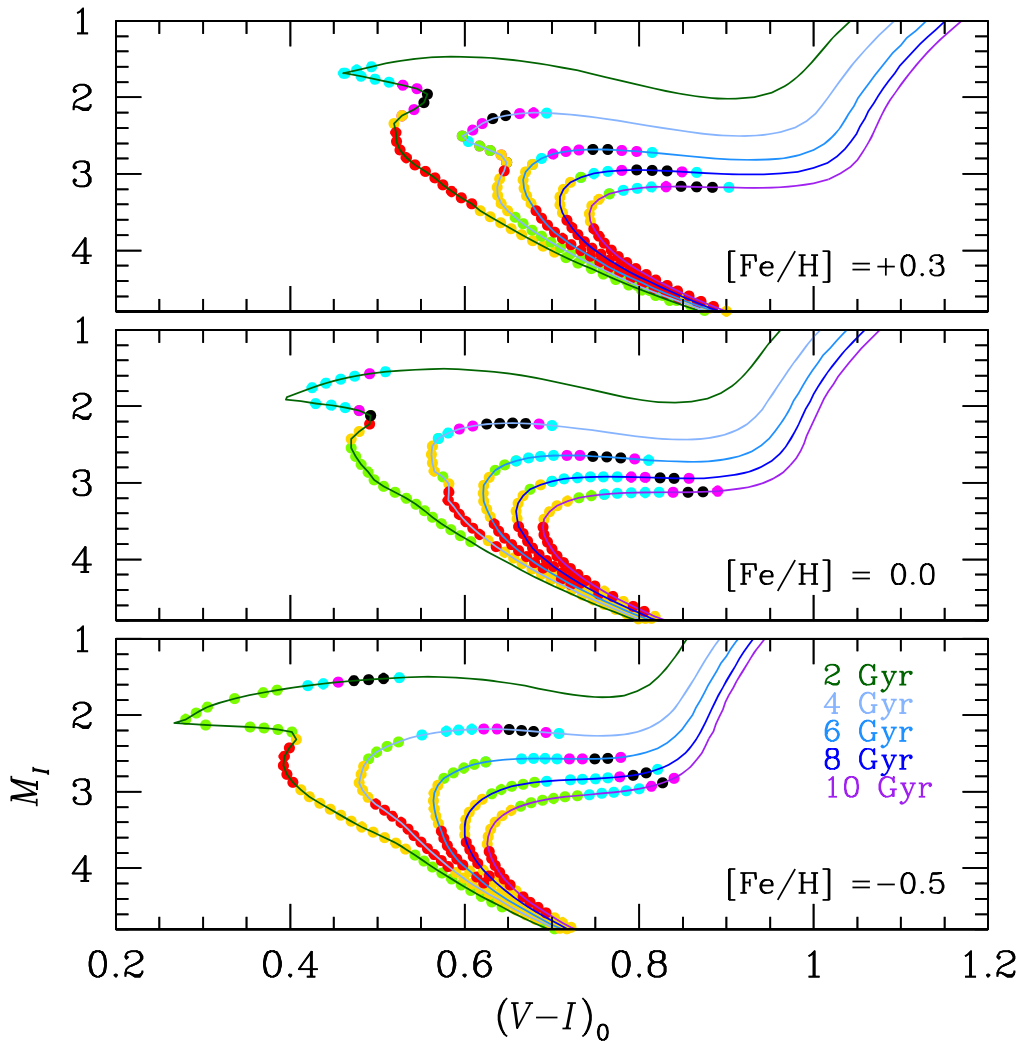


Figure 11. Positions of lens hosts and companions on 15 model isochrones from the accepted events. In each panel, the dots in red, yellow, and green and in black, magenta, and cyan are the 1σ , 2σ , and 3σ positions of the host and its companion, respectively.

probability of systems that contain a subgiant-branch star. Recall that if the stellar companion were on the main sequence for case (3) but on the subgiant branch for case (2), we would need to take account of the fact that main-sequence stars are more common than subgiants.

Now the companion is actually on the main sequence for the top two 2 Gyr isochrones, and it is on the turnoff for the metal-rich 4 Gyr isochrone. However, recall from Figure 10 that the former contributes negligibly, and the latter contributes $<1\%$. Even if this percentage were augmented by a factor of ~ 5 due to slower evolution on the turnoff, its contribution would still be small.

Thus, considering that both $[\text{Fe}/\text{H}] = 0.0$ and $+0.3$ can contribute to case (1), as discussed in Section 5.1, while $<5\%$ of stellar populations at these metallicities can contribute to cases (2) and (3), we estimate that from this quantitative analysis alone, the probability for cases (2) and (3) relative to case (1) is $p_d < 5\%$.

We now must take account of the fact that classes (A), (C), (D), and (E) can contribute to case (1), while classes (E) and (F) can contribute to cases (2) and (3). This contributes a

relative probability of $p_b/(1 - p_b) = (0.05 \times 0.84 + 0.01 \times 1.9)/(0.36 + 0.28 + 0.10 + 0.05) = 0.077$, i.e., $p_b = 7\%$. Therefore, the total probability that the host dominates the blended light is $(1 - p_d \times p_b) > 99.6\%$.

Finally, we ask why the quantitative analysis gave much more certainty ($>99.6\%$) that the host dominates the blended light than the qualitative analysis. The primary reason is that in the qualitative analysis, we implicitly assumed that, for most cases, there would be some isochrone that could provide the extra light from a turnoff/subgiant star that could be added to the host to make the observed blended light. However, Figure 10 shows that this is not the case.

6. Discussion

We have shown that the bright, relatively blue $[(V - I), I] \sim (1.8, 15.8)$ blended light is very likely to be primarily due to the host. The blend, and thus almost certainly the host, can be basically characterized immediately from a medium-resolution spectrum taken on a 4 or even 2 m class telescope. This would also provide a first epoch for the RV signatures of a putative stellar companion to the blend.












Moreover, by taking a high-resolution spectrum on an 8 m class telescope (similar to those obtained by Bensby et al. 2013), one could make a very detailed study of the chemical composition, age, and mass of the blend/host.

Finally, future RV observations with 30 m class telescopes could potentially detect and further characterize the planet. For example, let us assume that host and planet have $(M, m_p, a_\perp) = (1.16 M_\odot, 0.74 M_J, 4.5 \text{ au})$, as in the example of the 6 Gyr, $[\text{Fe}/\text{H}] = 0.0$ isochrone analyzed in Section 5.1. Then, we may estimate a semimajor axis, $a = \sqrt{3/2} a_\perp = 5.5 \text{ au}$, i.e., very similar to our own Jupiter. In this case, the period would be $P = 12 \text{ yr}$, and the reflex velocity of the host would be $v = 8.5 \text{ m s}^{-1}$. While the amplitude of this variation will be further reduced by $v \rightarrow v \sin i$, it should still be measurable on 30 m class telescopes. Because we already know q , these measurements would enable determination of the inclination angle i , in addition to the period P and the eccentricity e , which are rarely, if ever, possible for microlensing planets.

The object OGLE-2018-BLG-1269Lb is the second microlensing planet with a bright blue host for which such spectroscopic studies on 30 m telescopes will be possible. The first was OGLE-2018-BLG-0740b (Han et al. 2019), which also had a bright blue blend due to an $\sim 1.0 M_\odot$ host. In that case, the host was more than 1 mag fainter in the I band but just 0.65 mag fainter in the V band compared to OGLE-2018-BLG-1269Lb. On the other hand, the planet–host mass ratio q was substantially larger, leading to an estimated reflex velocity v that was 7.5 times larger. Taking all of these factors into account, OGLE-2018-BLG-0740Lb and OGLE-2018-BLG-1269Lb are comparably feasible for future RV studies.³⁵

This research has made use of the KMTNet system operated by the Korea Astronomy and Space Science Institute (KASI), and the data were obtained at the three host sites of CTIO in Chile, SAAO in South Africa, and SSO in Australia. A.G. was supported by JPL grant 1500811. Work by C.H. was supported by grants of the National Research Foundation of Korea (2017R1A4A1015178 and 2019R1A2C2085965). The OGLE has received funding from the National Science Centre, Poland, grant MAESTRO 2014/14/A/ST9/00121 to A.U. The MOA project is supported by JSPS KAKENHI grant Nos. JSPS24253004, JSPS26247023, JSPS23340064, JSPS15H00781, JP16H06287, and 19KK0082.

ORCID iDs

Youn Kil Jung  <https://orcid.org/0000-0002-0314-6000>
 Andrzej Udalski  <https://orcid.org/0000-0001-5207-5619>
 Jennifer C. Yee  <https://orcid.org/0000-0001-9481-7123>
 Cheongho Han  <https://orcid.org/0000-0002-2641-9964>
 Sun-Ju Chung  <https://orcid.org/0000-0001-6285-4528>
 Kyu-Ha Hwang  <https://orcid.org/0000-0002-9241-4117>
 Yoon-Hyun Ryu  <https://orcid.org/0000-0001-9823-2907>
 In-Gu Shin  <https://orcid.org/0000-0002-4355-9838>
 Yossi Shvartzvald  <https://orcid.org/0000-0003-1525-5041>
 Wei Zhu  <https://orcid.org/0000-0003-4027-4711>
 Weicheng Zang  <https://orcid.org/0000-0001-6000-3463>

Hyoun-Woo Kim  <https://orcid.org/0000-0001-8263-1006>
 Seung-Lee Kim  <https://orcid.org/0000-0003-0562-5643>
 Chung-Uk Lee  <https://orcid.org/0000-0003-0043-3925>
 Richard W. Pogge  <https://orcid.org/0000-0003-1435-3053>
 Jan Skowron  <https://orcid.org/0000-0002-2335-1730>
 Paweł Pietrukowicz  <https://orcid.org/0000-0002-2339-5899>
 Krzysztof Ulaczyk  <https://orcid.org/0000-0001-6364-408X>
 Patryk Iwanek  <https://orcid.org/0000-0002-6212-7221>
 Richard Barry  <https://orcid.org/0000-0003-4916-0892>
 David P. Bennett  <https://orcid.org/0000-0001-8043-8413>
 Akihiko Fukui  <https://orcid.org/0000-0002-4909-5763>
 Yoshitaka Itow  <https://orcid.org/0000-0002-8198-1968>
 Iona Kondo  <https://orcid.org/0000-0002-3401-1029>
 Naoki Koshimoto  <https://orcid.org/0000-0003-2302-9562>
 Shota Miyazaki  <https://orcid.org/0000-0001-9818-1513>
 Clément Ranc  <https://orcid.org/0000-0003-2388-4534>
 Nicholas J. Rattenbury  <https://orcid.org/0000-0001-5069-319X>
 Daisuke Suzuki  <https://orcid.org/0000-0002-5843-9433>

References

- Alard, C., & Lupton, R. H. 1998, *ApJ*, 503, 325
 Albrow, M. D., Horne, K., Bramich, D. M., et al. 2009, *MNRAS*, 397, 2099
 Alcock, C., Allsman, R. A., Alves, D. R., et al. 2001, *Natur*, 414, 617
 Batista, V., Beaulieu, J.-P., Bennett, D. P., et al. 2015, *ApJ*, 808, 170
 Batista, V., Gould, A., Dieters, S., et al. 2011, *A&A*, 529, 102
 Beaulieu, J.-P., Bennett, D. P., Batista, V., et al. 2016, *ApJ*, 824, 83
 Bennett, D. P., Bhattacharya, A., Anderson, J., et al. 2015, *ApJ*, 808, 169
 Bennett, D. P., Bhattacharya, A., Beaulieu, J. P., et al. 2020, *AJ*, 159, 68
 Bennett, D. P., Rhie, S. H., Nikolaev, S., et al. 2010, *ApJ*, 713, 837
 Bensby, T., Yee, J. C., Feltzing, S., et al. 2013, *A&A*, 549, 147
 Bessell, M. S., & Brett, J. M. 1988, *PASP*, 100, 1134
 Bhattacharya, A., Beaulieu, J.-P., Bennett, D. P., et al. 2018, *AJ*, 156, 289
 Bond, I. A., Abe, F., Dodd, R. J., et al. 2001, *MNRAS*, 327, 868
 Dominik, M. 1998, *A&A*, 329, 361
 Duquenoey, A., & Mayor, M. 1991, *A&A*, 248, 485
 Gaia Collaboration, Brown, A. G. A., Vallenari, A., et al. 2018, *A&A*, 616, 1
 Gaia Collaboration, Prusti, T., de Bruijne, J. H. J., et al. 2016, *A&A*, 595, A1
 Gaudi, B. S., Bennett, D. P., Udalski, A., et al. 2008, *Sci*, 319, 927
 Gould, A. 1992, *ApJ*, 392, 442
 Gould, A. 2000, *ApJ*, 542, 785
 Griest, K., et al. 1991, *ApJL*, 372, L79
 Han, C., Jung, Y. K., Udalski, A., et al. 2018, *ApJ*, 867, 136
 Han, C., Yee, J. C., Udalski, A., et al. 2019, *AJ*, 158, 102
 Hirao, Y., Bennett, D. P., Ryu, Y.-H., et al. 2020, *AJ*, 160, 74
 Jung, Y. K., Gould, A., Zang, W., et al. 2019, *AJ*, 157, 72
 Jung, Y. K., Udalski, A., Gould, A., et al. 2018, *AJ*, 155, 219
 Jung, Y. K., Udalski, A., Sumi, T., et al. 2015, *ApJ*, 798, 123
 Kervella, P., Bersier, D., Mourard, D., et al. 2004, *A&A*, 428, 587
 Kim, D.-J., Kim, H.-W., Hwang, K.-H., et al. 2018, *AJ*, 155, 76
 Kim, S.-L., Lee, C.-U., Park, B.-G., et al. 2016, *JKAS*, 49, 37
 Koshimoto, N., Bennett, D. P., & Suzuki, D. 2020, *AJ*, 159, 268
 Kozłowski, S., Woźniak, P. R., Mao, S., & Wood, A. 2007, *ApJ*, 671, 420
 Luri, X., Brown, A. G. A., Sarro, L. M., et al. 2018, *A&A*, 616, A9
 Nataf, D. M., Gould, A., Fouqué, P., et al. 2013, *ApJ*, 769, 88
 Paczyński, B. 1986, *ApJ*, 304, 1
 Paczyński, B. 1991, *ApJL*, 371, L63
 Ryu, Y.-H., Navarro, M. G., Gould, A., et al. 2019, *AJ*, 159, 58
 Spada, F., Demarque, P., Kim, Y.-C., et al. 2017, *ApJ*, 838, 161
 Sumi, T., Abe, F., Bond, I. A., et al. 2003, *ApJ*, 591, 20
 Szymański, M. K., Udalski, A., Soszyński, I., et al. 2011, *AcA*, 61, 83
 Tomaney, A. B., & Crofts, A. P. S. 1996, *AJ*, 112, 2872
 Udalski, A. 2003, *AcA*, 53, 291
 Udalski, A., Szymański, M. K., & Szymański, G. 2015, *AcA*, 65, 1
 Vandorou, A., Bennett, D. P., Beaulieu, J.-P., et al. 2020, *AJ*, 160, 121
 Woźniak, P. R. 2000, *AcA*, 50, 421
 Yee, J. C., Johnson, J. A., Skowron, J., et al. 2016, *ApJ*, 821, 121
 Yoo, J., DePoy, D. L., Gal-Yam, A., et al. 2004, *ApJ*, 603, 139
 Zinn, J. C., Pinsonneault, M. H., Huber, D., & Stello, D. 2019, *ApJ*, 878, 136

³⁵ The first microlensing planets for which 30 m telescope RV studies were proposed were OGLE-2006-BLG-109Lb,c. At $M = 0.5 M_\odot$, their host is much less massive and hence much redder and fainter than either of the bright blue hosts discussed here. Nevertheless, Bennett et al. (2010) estimated that the host had $H_I = 17.2$ and so proposed that it would be possible to monitor it in the infrared with 30 m telescopes.